



Originally published as:

Mulcahy, P., Chen, C., Kay, S. M., Brown, L. D., Isacks, B. L., Sandvol, E., Heit, B., Chen, Y., Coira, B. L. (2014): Central Andean mantle and crustal seismicity beneath the Southern Puna plateau and the northern margin of the Chilean-Pampean flat slab. - *Tectonics*, 33, p. 1636-1658.

DOI: <http://doi.org/10.1002/2013TC003393>

## RESEARCH ARTICLE

10.1002/2013TC003393

## Key Points:

- Wadati-Benioff geometry under Southern Puna and Chilean flat slab revised
- Crustal focal mechanisms support E-W compression and N-S extension
- Seismicity supports lithospheric delamination under Southern Puna

## Supporting Information:

- Readme
- Appendix S1
- Appendix S2
- Appendix S3
- Appendix S4
- Appendix S5
- Appendix S6
- Appendix S7
- Appendix S8

## Correspondence to:

S. M. Kay,  
smk16@cornell.edu

## Citation:

Mulcahy, P., C. Chen, S. M. Kay, L. D. Brown, B. L. Isacks, E. Sandvol, B. Heit, X. Yuan, and B. L. Coira (2014), Central Andean mantle and crustal seismicity beneath the Southern Puna plateau and the northern margin of the Chilean-Pampean flat slab, *Tectonics*, 33, 1636–1658, doi:10.1002/2013TC003393.

Received 25 JUN 2013

Accepted 3 AUG 2014

Accepted article online 11 AUG 2014

Published online 27 AUG 2014

## Central Andean mantle and crustal seismicity beneath the Southern Puna plateau and the northern margin of the Chilean-Pampean flat slab

Patrick Mulcahy<sup>1,2</sup>, Chen Chen<sup>1,2</sup>, Suzanne M. Kay<sup>1</sup>, Larry D. Brown<sup>1</sup>, Bryan L. Isacks<sup>1</sup>, Eric Sandvol<sup>3</sup>, Benjamin Heit<sup>4</sup>, Xiaohui Yuan<sup>4</sup>, and Beatriz L. Coira<sup>5</sup>

<sup>1</sup>Earth and Atmospheric Sciences, Cornell University, Ithaca, New York, USA, <sup>2</sup>Shell Exploration Company, New Orleans, Louisiana, USA, <sup>3</sup>Geological Sciences, University of Missouri, Columbia, Missouri, USA, <sup>4</sup>Deutsches GeoForschungsZentrum GFZ, Potsdam, Germany, <sup>5</sup>CONICET, Instituto de Geología y Minería, San Salvador de Jujuy, Argentina

**Abstract** Earthquake hypocenters recorded in the Andean Southern Puna seismic array (25–28°S, 70–65°W) provide new constraints on the shape of the subducting Nazca plate beneath the Puna plateau, the transition into the Chilean-Pampean flat slab and the thermal state of the mantle and crust. Some 270 new mantle hypocenters suggest that the subducting slab under the Puna shoals into the flat-slab segment more abruptly and farther to the north than previously indicated. The revised geometry is consistent with the Central Volcanic Zone Incaipillo caldera being the southernmost center with Pleistocene activity until reaching the southern side of the flat-slab region. Evidence for the revised slab geometry includes three well-defined hypocenter clusters in the Pipanaco nest (27.5–29°S, 68–66°W), which are interpreted to reflect slab-bending stresses. A few low-magnitude earthquakes with strongly attenuated *S* waves in the long-recognized Antofalla teleseismic gap (25.5–27.5°S) support a continuous slab under the Southern Puna. The paucity of gap earthquakes and the presence of mafic magmas are consistent with a hot mantle wedge reflecting recent lithospheric delamination. Evidence for a hot overlying Puna crust comes from new crustal earthquake hypocenters concentrated at depths shallower than 5 km. Two notable short-duration swarms were recorded under the resurgent dome of the ~2 Ma back-arc Cerro Galán caldera and the near-arc Cerro Torta dome. New crustal earthquake focal mechanisms from 17 events in the array along with two existing mechanisms have strike slip, oblique reverse, and oblique normal solutions fitting with regional E-W compression and N-S extension.

### 1. Introduction

The central Andean Puna-Altiplano Plateau, which is the world's second largest continental plateau, is bounded to the south by the Chilean-Pampean flat slab and to the north by the Peruvian flat slab (Figure 1). Unlike the larger Tibetan Plateau, which is associated with India-Asia continental collision, the Andean Plateau is interpreted to reflect collision of a regionally shallow but a variably dipping subducting Nazca oceanic plate with South America [e.g., Isacks, 1988]. The giant late Neogene ignimbrite volcanic centers, erupted through the thick crust of the Puna-Altiplano plateau, have been correlated with episodes of delamination of crust and mantle lithosphere over shallowing portions of the subducting slab [e.g., Kay and Coira, 2009]. The uplift and crustal thickening under the plateau are generally largely attributed to crustal shortening [e.g., Isacks, 1988; Allmendinger et al., 1997; Oncken et al., 2006].

Seismic data have played a major role in defining the variable shape of the Wadati-Benioff zone [e.g., Cahill and Isacks, 1992], the crustal and mantle lid thickness, and the mechanical and thermal state of the lithosphere and asthenosphere under the central Andes. To supplement teleseismic data, the northern Puna and Altiplano plateau regions have been the sites of local seismic arrays (Figure 1) including the Panda Jujuy [e.g., Cahill et al., 1992], Andean Continental Research Project [ANCORP Working Group, 2003], CINCA [e.g., Husen et al., 1999], BANJO [Swenson et al., 2000], PUNA '97 [Yuan et al., 2002], and PISCO '94 [e.g., Graeber and Asch, 1999] arrays. These studies show that the crust under the Altiplano is among the thickest (~80 km) on Earth [e.g., Beck and Zandt, 2002; Yuan et al., 2002; McGlashan et al., 2008; Heit et al., 2008], whereas the Puna includes some of the thinnest crust on the plateau (~45 km) as inferred from gravity [Whitman, 1994; Tassara et al., 2006] and seismic studies [e.g., Yuan et al., 2002; Heit et al., 2014]. The studies also provide evidence for an irregular lithospheric base and show high-velocity regions in the mantle wedge, which are interpreted as delaminated lithosphere [e.g., Schurr et al., 2006].

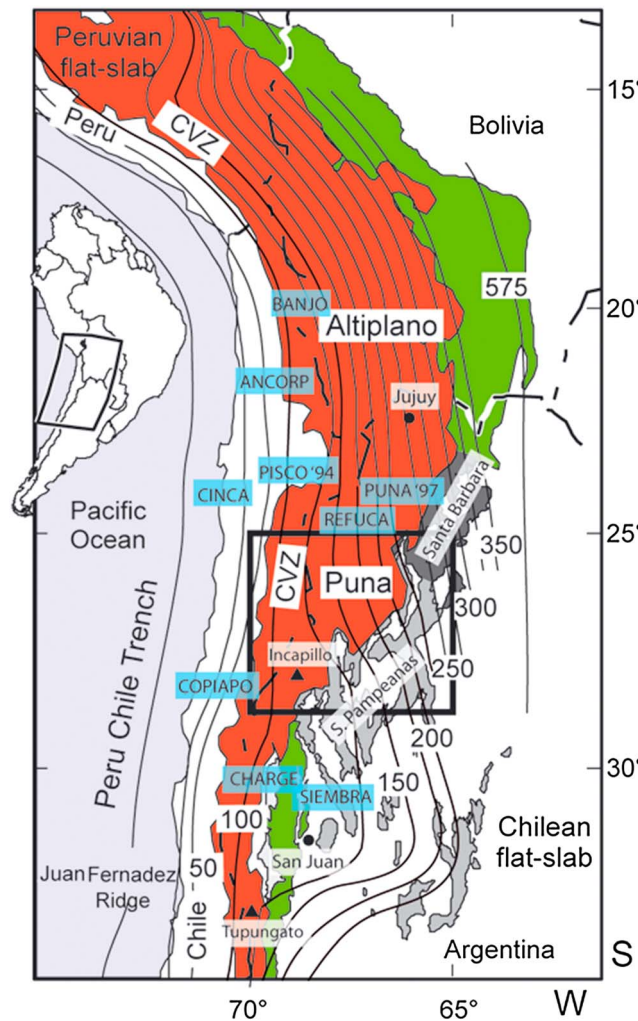


**Figure 1.** Map of the central Andes modified from Allmendinger *et al.* [1997]. Red areas have elevations over 3700 m, green areas are thin-skinned fold and thrust belts, gray areas are thick-skinned uplifts of the high-angle reverse fault bounded Sierras Pampeanas, and dark gray area is the Santa Barbara thrust belt characterized by inverted Mesozoic normal faults. The Central Volcanic Zone (CVZ) Incapillo and Southern Volcanic Zone (SVZ) Tupungato centers are the arc volcanic centers with post late Miocene activity that are nearest to the margins of the amagmatic Chilean-Pampean flat slab. The region of the Southern Puna seismic experiment with the generalized Wadati-Benioff zone contours defined in this study is enclosed by the black rectangle. Contours elsewhere are from Cahill and Isacks [1992]. Regions of seismic arrays mentioned in the text are labeled in blue. Black circles are major cities.

contours from the Southern Puna into the Chilean-Pampean flat slab, (b) assess the distribution of Wadati-Benioff zone earthquakes relative to the curvature and thermal state of the subducting Nazca slab, and (c) analyze the distribution of crustal earthquakes and swarms and infer the current crustal stress regime under the Southern Puna plateau. The analysis leads to a revised Wadati-Benioff geometry under the Southern Puna and northernmost Chilean-Pampean flat slab and insights into the aftermath of lithospheric delamination under the Southern Puna.

## 2. Regional Geophysical and Geologic Setting of the Southern Puna

The Southern Puna plateau spans the area from ~24°S to 28°S and 66° to 70°W (see Figures 1 and 2) and is the southernmost part of the Puna-Altiplano plateau in the Central Andes. The geologic and geophysical

The Southern Puna and its transition to the Chilean-Pampean flat-slab region have been far less studied. The results discussed here focus on local earthquakes recorded in the 2007–2009 Southern Puna seismic (also called PUDEL) experiment that covered the region from 24°S to 28°S and 66° to 70°W (Figures 1–3). The area spans the Southern Puna and straddles the transition from the ~30° dipping subducting Nazca plate under the Southern Puna to the northernmost part of the Chilean-Pampean flat slab (Figure 1). The Southern Puna includes the Cerro Galán ignimbrite complex (Figure 2) and mafic volcanic centers, whose formations have been suggested to be related to lithospheric delamination [e.g., Kay *et al.*, 1994, 2011]. The only previous seismic arrays in the area were the temporary Receiver Function Central Andes (ReFuCA) array near 25.5°S (Figure 3) [Woelber *et al.*, 2009] that paralleled the northern boundary of the Southern Puna array and an array near Copiapó in Chile between 26.5°S and 28.5°S that targeted nearer-trench features west of 69.5°W [Comte *et al.*, 2002]. The Chile Argentina Geophysical Experiment (CHARGE) [e.g., Anderson *et al.*, 2007] and Sierras Pampeanas Experiment using a Multicomponent Broadband Array (SIEMBRA) [e.g., Gans *et al.*, 2011] arrays over the Chilean-Pampean flat-slab region to the south are separated from the Southern Puna array by a gap at 28°S to 30°S.

In this paper, we report the locations of the mantle and crustal earthquakes recorded by the Southern Puna seismic array. We use these new events to (a) redefine the Wadati-Benioff zone

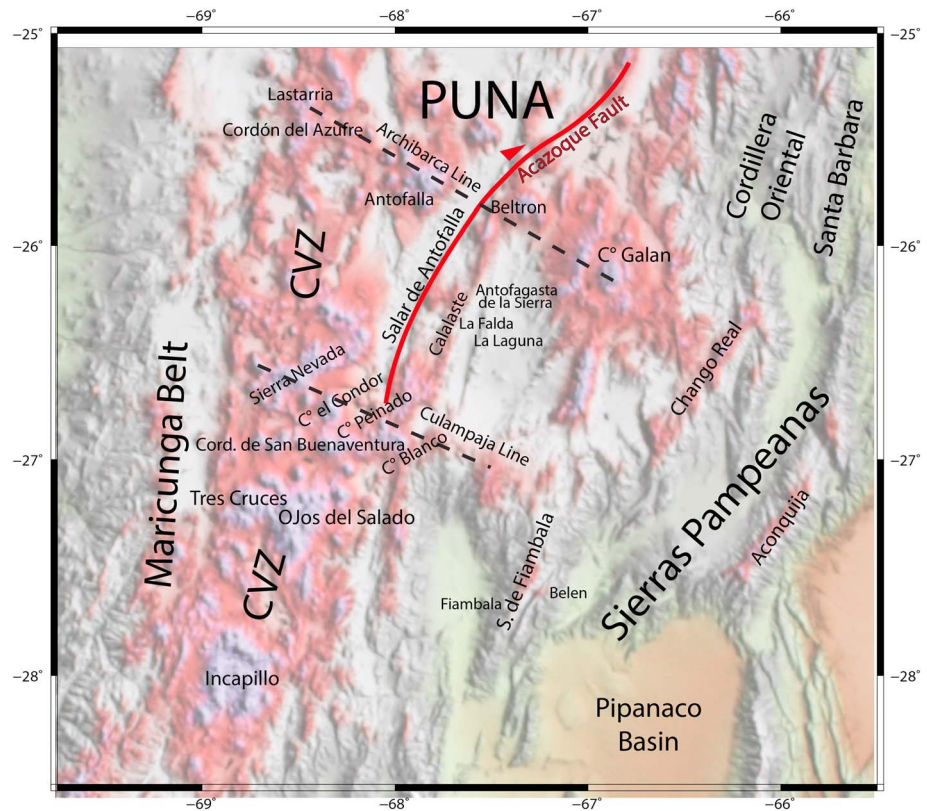


**Figure 2.** Satellite radar topographic mission (SRTM) image of the general region of the Southern Puna seismic experiment with geographic regions mentioned in the text. The right-lateral strike-slip Acázoque Fault is shown in red, and the Archibarca and Culampaja volcanic lines are denoted by black dashed lines.

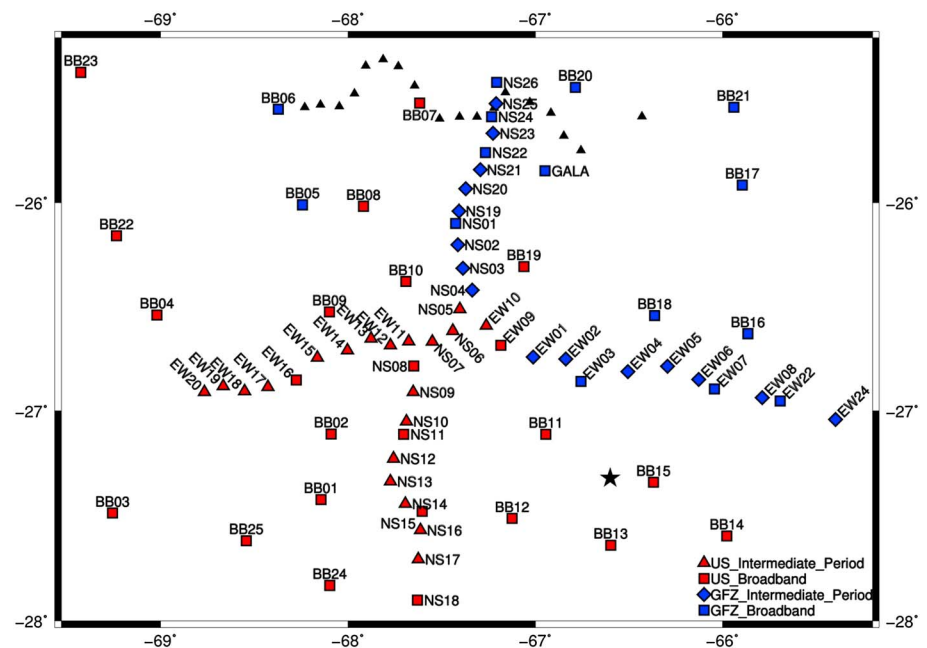


**Figure 3.** Map of the Southern Puna seismic array. Squares mark sites of broadband seismometers and diamonds sites of intermediate-period seismometers. Small black triangles near 25.5°S mark sites of seismic station in the ReFuCa experiment [Woelber *et al.*, 2009]. The Bajo de la Alumbreira mine, whose blasts were used as a control on earthquake locations, is marked by the star.

setting and magmatic history of the region have been reviewed by *Allmendinger et al.* [1997] and *Kay and Coira* [2009], among others. The western boundary of the Southern Puna plateau is marked by Neogene arc volcanic centers, whose heights rise to over 6300 m in the 27–6 Ma Maricunga Belt arc in the west and the Pleistocene to Holocene Central Volcanic Zone (CVZ) arc to the east (Figure 2). The southern end of the young CVZ arc near 28°S terminates at the Incapillo volcanic complex, whose youngest age of 0.5 Ma [*Goss et al.*, 2009] marks the last post-Miocene volcanic activity until reaching the Southern Volcanic Zone (SVZ) Tupungato volcano near 33.2°S to the south of the Chilean-Pampean flat slab (Figure 1). The eastward arc front displacement from the Maricunga Belt to the CVZ at 8–3 Ma has been suggested to be associated with fore-arc subduction erosion during the shallowing of the Chilean-Pampean flat slab [*Kay and Mpodozis*, 2002; *Goss et al.*, 2013]. *Yañez et al.* [2001] among others suggest that the slab shallowing is linked to the near-normal subduction of the Juan Fernandez Ridge on the Nazca plate, which began after ~10 Ma.

The Southern Puna itself is marked by NW trending lines of major volcanic centers (Figure 2). The northern Archibarca line runs from the active CVZ Lastarria volcano through the 14–4 Ma Antofalla and Beltran stratovolcanic complexes [e.g., *Coira and Pezzutti*, 1976; *Coira et al.*, 1993; *Richards et al.*, 2006] to the ~6.5–2 Ma giant Cerro Galán ignimbrite complex [e.g., *Sparks et al.*, 1985; *Folkes et al.*, 2011; *Kay et al.*, 2011]. The Culampaja line to the south runs from the CVZ Sierra Nevada, Cerro Condor, and Cerro Peinado volcanoes to the < 1 Ma Cerro Blanco volcanic complex. A west to east trending chain of young volcanic domes in the fault-controlled Cordillera de San Buenaventura also terminates near Cerro Blanco. Elevations in the back arc range from over 6300 m at Cerro Galán to 3500 m in the intervening regions.

The Southern Puna is also crossed by north and northeast trending strike-slip faults with normal and reverse components, the most prominent of which is the Acazoque fault [e.g., *Chinn and Isacks*, 1983] (Figure 2) that bounds the Salar de Antofalla. Mafic ~6.5 to 0 Ma monogenetic volcanic centers like La Falda and La Laguna occur along these faults north, south, and west of Cerro Galán [e.g., *Kay et al.*, 1994; *Risse et al.*, 2008]. The Southern Puna is bordered by the Cordillera Oriental fold-thrust belt, which gives way to the Santa Barbara thrust system in the east and the Sierras Pampeanas to the south (see Figures 1 and 2).

Previous geophysical studies provide initial estimates of the shape of the Wadati-Benioff seismic zone, the distribution of earthquake hypocenters, and lithospheric and crustal thicknesses under the Southern Puna. *Cahill and Isacks* [1992] presented contours of the Wadati-Benioff zone based on teleseismic data selected from global catalogs and emphasized the scarcity of intermediate-depth mantle earthquakes under the Southern Puna in the area called the Antofalla teleseismic gap. More recent representations of the contours based on visual or automated interpolations of global teleseismic data [e.g., *Gudmundsson and Sambridge*, 1998; *Syracuse and Abers*, 2006; *Hayes et al.*, 2012] provide no significant improvement in resolution over the *Cahill and Isacks* [1992] model in the region considered here. *Whitman et al.* [1992, 1996] used data from a local seismic array near San Juan at 32°S and the temporary northern Puna Panda array near 23°S to argue for continuity of the slab based on seismic wave propagation through the Antofalla teleseismic gap. The same authors used observations from strong *S<sub>n</sub>* attenuation and topographic and gravity data to infer a much thinner mantle lid under the Southern Puna than under the plateau to the north. *Febrer et al.* [1982] also inferred a thin lithosphere and hot mantle wedge in this region based on a magnetotelluric study. *Kay and Kay* [1993] and [*Kay et al.*, 1994] used these observations along with temporal and spatial changes in magmatic patterns and the structural data of *Marrett et al.* [1994] to argue for lower crustal and mantle lithospheric delamination under the Southern Puna.

Like *Whitman* [1994], *Tassara et al.* [2006] postulated a relatively thin crust and lithosphere under the Southern Puna near 25°S based on gravity data. *McGlashan et al.* [2008] used depth phase (pP) precursors from large teleseismic slab earthquakes to indicate a thick crust (>65 km) within the Southern Puna array near 28°S, 68.5°W and like *Yuan et al.* [2002] documented a thick crust (~58–75 km) to the north with a locally thinned crust near ~25°S, 67.5°W (42–49 km). *Woelbern et al.* [2009] used tomography and receiver functions from the ReFuCa array (Figures 1 and 3) to argue for pronounced low-velocity anomalies under the plateau near 25.5°S. More recently, *Bianchi et al.* [2013] used Southern Puna array data to create *P* wave tomographic images exhibiting low-velocity crustal and mantle seismic anomalies across the Southern Puna. Additional evidence for relatively low crustal and mantle seismic velocities and substantial variations in crustal thickness under the Southern Puna comes from attenuation and surface wave tomography, shear wave splitting mapping, and receiver function studies using Southern Puna array data [*Liang et al.*, 2014; *Calixto Mory et al.*, 2013; *Heit et al.*, 2014].

### 3. Southern Puna Seismic Experiment

The earthquakes used in the analyses here were mostly recorded by the Southern Puna array, which was primarily designed to acquire seismic data to image the character of the crust and mantle under the Southern Puna and the transition into the Chilean-Pampean flat-slab region. Participants in the experiment were from Cornell University, University of Missouri, the German GeoForschungsZentrum, University of Chile, the Argentine National Universities of Jujuy, San Juan, Buenos Aires, and Catamarca, and Servicio Geológico Minero Argentino (SEGEMAR) and National Institute for Seismic Prevention (INPRES) in Argentina.

The Southern Puna array consisted of 74 seismic stations that recorded continuously from December 2007 to October 2009 and were deployed in an area bounded by 25°S and 28°S and 65°W and 70°W (Figures 1 and 3). The instruments included 12 CMG 40-T, 7 CMG 3-T, 6 Nanometrics Trillium 40S and 7 Trillium 120S, and 10 STS-2 sensors from Incorporated Research Institutions for Seismology-Program for Array Seismic Studies of the Continental Lithosphere (IRIS-PASSCAL), Universities of Missouri, St. Louis, and Chile, and 30 CMG 3ESP and Mark L4 sensors from the GeoForschungsZentrum. Of these, 35 intermediate period and 13 broadband instruments were installed in trench-parallel (north-south) and trench-perpendicular (east-west) trending transects with 10–20 km spacing and with broadband instruments approximately at every fourth station. The 39 broadband stations formed a regional network with a spacing of ~35 to 50 km. Station coordinates and names are listed in Appendix S1 in the supporting information, and continuous waveform data are archived at the IRIS Data Management Facility and the GEOFON data center.

#### 3.1. Earthquake Locations

Most of the earthquakes analyzed from the Southern Puna array document activity in a region for which very few teleseismic events are listed in the global catalogs of the Preliminary Determination of Episodes (PDE), ISC [International Seismological Centre, 2010], and NEIC (National Earthquake Information Center of the U.S. Geological Survey) as shown on Figure 4. Individual records were visually examined to minimize omission of small-magnitude or unusual waveform events. The continuous data files were subdivided into hour-long increments and displayed using the SEISAN program (L. Ottemöller, et al., Seisan earthquake analysis software for windows, solaris, linux and macosx, 2014, <http://seis.geus.net/software/seisan/seisan.html>) for event picking and subsequent analysis. Phase picks were made on unfiltered seismograms where possible. For noisier records, a 1–5 Hz band-pass filter was applied to enhance body wave arrivals. When available, both *P* and *S* wave arrivals were used for locations. Approximately 60% of the stations showed recognizable *S* wave arrivals for a typical earthquake. Significant variations in the amplitudes of the observed *S* waves and their absence on some records are attributed to local areas of strong *S* wave attenuation within the array [see Liang et al., 2014].

Hypocenters were calculated using the HYP program option [Lienert and Haskov, 1995] in the SEISAN software package. Earthquakes used in this study were identified on at least 15 stations and had resulting RMS traveltimes residual errors of less than 1.5 s. Events located within the array were judged to be most accurate when consistent with the suggestion of Bondar et al. [2004] that local networks can locate earthquakes to within 5 km, given adequate azimuthal coverage and including at least 10 stations within 250 km and at least one station within 30 km (i.e., for depth control). The ~500 earthquakes meeting these criteria along with their location error estimates are listed in Appendix S2. The average “raw” depth error for all is 18 km. If the 16 locations with depth errors over 100 km are excluded, the average error falls to 11.6 km, and if those with errors over 50 km are excluded (25 more), the average is 10.3 km. The average radial error is 10.2 km (only 36 events yield a formal error > 20 km). An intrinsic concern is possible systematic error from uncertainty in the velocity structure used for the locations.

At the time of our initial analysis, there was virtually no crustal velocity information for the region. Thus, we bootstrapped a one-dimensional velocity model using the observed traveltimes corresponding to initial event locations for the 14 well-located regional earthquakes in Table 1. These data were supplemented with traveltimes from more distant, but less accurately located regional events in order to define a *P<sub>n</sub>* phase to constrain a crustal thickness estimate. The resulting “bulk” crustal and upper mantle velocities derived from the least squares determined slopes of the *P<sub>g</sub>* and *P<sub>n</sub>* arrivals shown in Figure 5a are 6.0 (*P<sub>g</sub>*), 8.0 (*P<sub>n</sub>*), and 3.45 (*S<sub>g</sub>*), respectively. An average crustal thickness of 40 km was calculated using the well-known relationship for refraction from a single layer:  $t_h = (1/2) X_c [(a_2 - a_1)/(a_2 + a_1)]^{1/2}$ , where  $t_h$  is the crustal thickness,  $X_c$  is the crossover distance (210 km in Figure 5a),  $a_1$  is crustal velocity, and  $a_2$  is mantle velocity

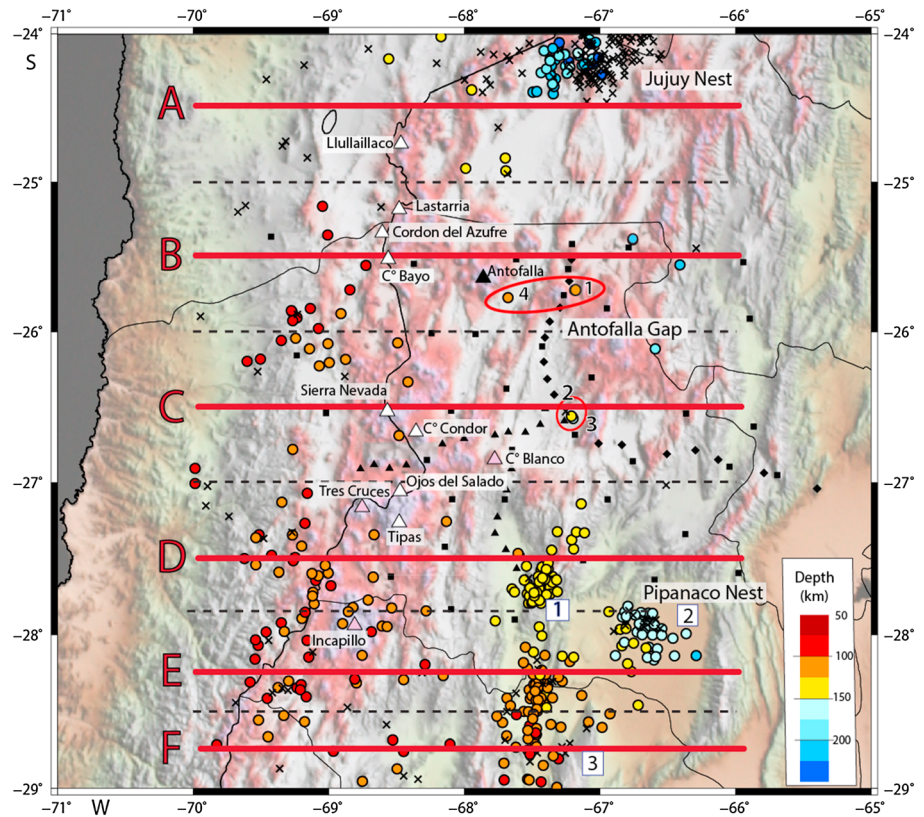


**Figure 4.** SRTM image with hypocenters recorded by the Southern Puna array indicated by circles color coded by depth in legend. Earthquakes satisfying the 40 station criteria from the ISC earthquake catalog for the deployment period are plotted as crosses. Labeled triangles indicate important active (white), recently active (violet), and inactive (black) volcanic centers. Locations of cross sections A to F in Figure 6 are indicated by labeled thick red lines. The white-backed numbers labeled 1, 2, and 3 refer to the three clusters of the Pipanaco earthquake nest. Earthquakes numbered 1 to 4 and circled in red in the Antofalla teleseismic gap are discussed in the text.

[e.g., *Lay and Wallace, 1995*]. This thickness is within the range (36–70 km) reported by *Heit et al. [2014]* from receiver functions analyses for the area. Velocities for the deeper mantle begin at 8.05 to and increase to 8.5 as shown in Figure 5b. This is called the initial model in this paper and in Appendix S3.

To evaluate the potential impact of laterally variable velocities on relocation accuracy across a region with crustal thicknesses varying from 35 to 70 km [*Heit et al., 2014*], the probable presence of eclogitic lower

**Table 1.** Earthquakes Used in Velocity Model Calculation

Year	Month	Day	Hour	Minute	Second	Latitude	Longitude	Depth	Stations
2008	3	6	12	19	22.1	-24.419	-65.039	15	57
2008	3	17	12	14	43.8	-24.844	-65.220	15	53
2008	3	23	14	34	19.0	-27.335	-66.587	0	51
2008	4	3	01	00	29.8	-28.667	-71.285	15	59
2008	5	6	06	52	10.9	-24.486	-69.868	15	59
2008	7	25	12	13	16.0	-28.180	-70.981	15	64
2008	10	30	01	32	48.5	-24.034	-70.105	15	51
2008	11	4	10	32	5.3	-27.854	-71.123	15	59
2008	12	5	03	49	21.0	-24.942	-65.485	15	64
2009	1	9	22	43	32.8	-23.039	-70.805	15	57
2009	2	6	02	58	38.3	-27.987	-71.104	15	61
2009	3	24	06	22	53.3	-28.251	-72.071	15	51
2009	3	26	18	16	33.8	-25.702	-70.454	15	49
2009	4	2	04	20	9.5	-27.486	-71.125	15	50

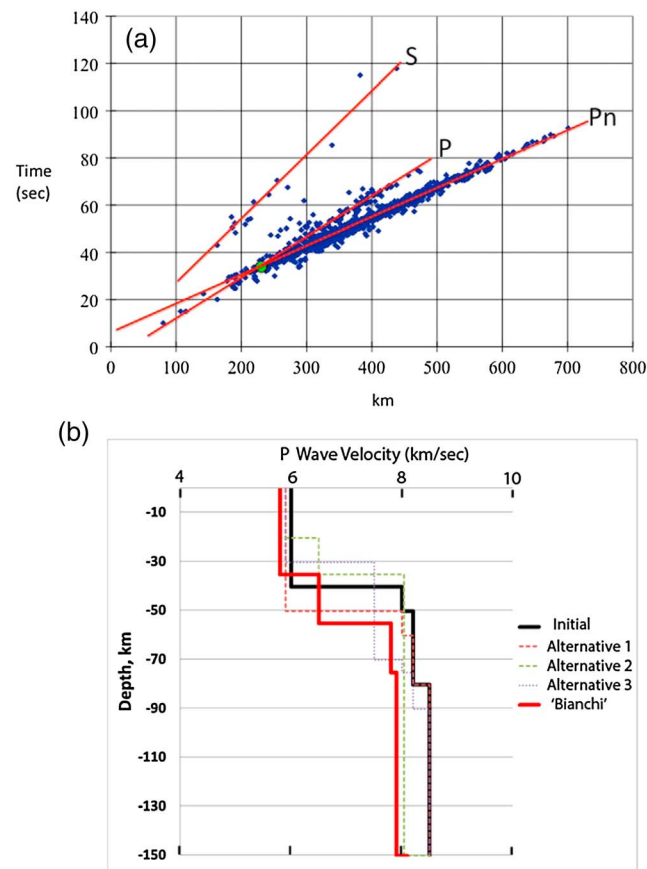


**Figure 5.** (a) *P* wave traveltimes versus distance plot for 14 regional earthquakes in Table 1 recorded by the Southern Puna seismic network and listed in catalogs. Red lines indicate best fit lines corresponding to *P*, *S*, and *Pn* phase arrivals. Green point denotes *P/Pn* crossover distance, which corresponds to a 40 km thick crust. Phase velocities given by slopes of red lines and crossover distance were used to construct a one-dimensional velocity model. *V<sub>p</sub>* is 6.0 km/s, *V<sub>s</sub>* is 3.45 km/s, and *Pn* is 8 km/s. The resulting *V<sub>p</sub>/V<sub>s</sub>* is 1.74. (b) *P* wave velocity models used to locate earthquakes in this study. The crustal segment of the original velocity model used is based on the wide-angle refraction model in Figure 5a. An average *P* wave velocity of 6 km/s is used to a depth of 40 km followed by the default velocities in the SEISAN program. The model in red (Bianchi model), based on the Bianchi *et al.* [2013] and Heit *et al.* [2014] studies, uses a 55 km thick crust with an increase in velocity at 35 km and mantle velocities in global models. Results from the alternative and Bianchi models are presented and discussed in Appendix S3.

crust in some regions and variable slab dips, these events were relocated with a suite of 1-D velocity models as shown in Figure 5b. Locations from the model with a variable velocity of 55 km thick crust with the mantle velocities used by Bianchi *et al.* [2013] and Heit *et al.* [2014] are compared with the initial model in the cross-section profiles in Figure 6, and the results of all of the models are compared in Appendix S3. In spite of the greater detail in the “Bianchi” model, the locations show significantly greater misfits to the data than in the original simpler velocity model. Given the limited nature of the hypocentral “shifts” in mantle events associated with these various velocity models as well as the inherent uncertainties associated with the various methodologies used to estimate velocity and crustal thickness variations beneath the array, we focus on the results of the initial model as shown in Figures 4, 6, and 8. In the text below, we point out where there could be significant differences depending on the velocity choice. The most significant depth divergences occur where the crust is thickest along the arc region at 68°W to 69°W. In that region, events can be ~ 10 km shallower with a 50 km as opposed to a 40 km thick crust.

Additional confidence in these locations, especially for shallow events using the initial model, is provided by mine blasts from the Bajo de la Alumbrera mine (Figure 3; 27.32°S, 66.60°W, elevation 2500 m). The blast epicenters were located to within 4 km of the mine and hypocentral depths to within 1 km using the initial model.

Magnitudes for the reported earthquakes were calculated where possible using the coda magnitude procedure in SEISAN. The coda length was picked on vertical component seismograms displayed at constant gain with a 1–5 Hz band-pass filter to ensure consistency between events. Calculated magnitudes for local events were compared to those available in the ISC and NEIC catalogs to ensure proper calibration of the coda magnitude procedure.

### 3.2. Mantle Earthquake Identification and Distribution

Using the data recorded in the Southern Puna array, we identified and located over 1000 earthquakes deeper than 50 km in the region of the array. Of these, 271 satisfied our “good” criteria of being recorded on more than 15 stations with a RMS time residual less than 1.5 s. If the worst three using the initial model are treated as outliers, the corresponding horizontal position errors for the remaining 268 range from 2.1 to 23.3 km (average 8.5 km) with depth errors of 2.5 to 36.5 km (average 10.4 km). Over the same

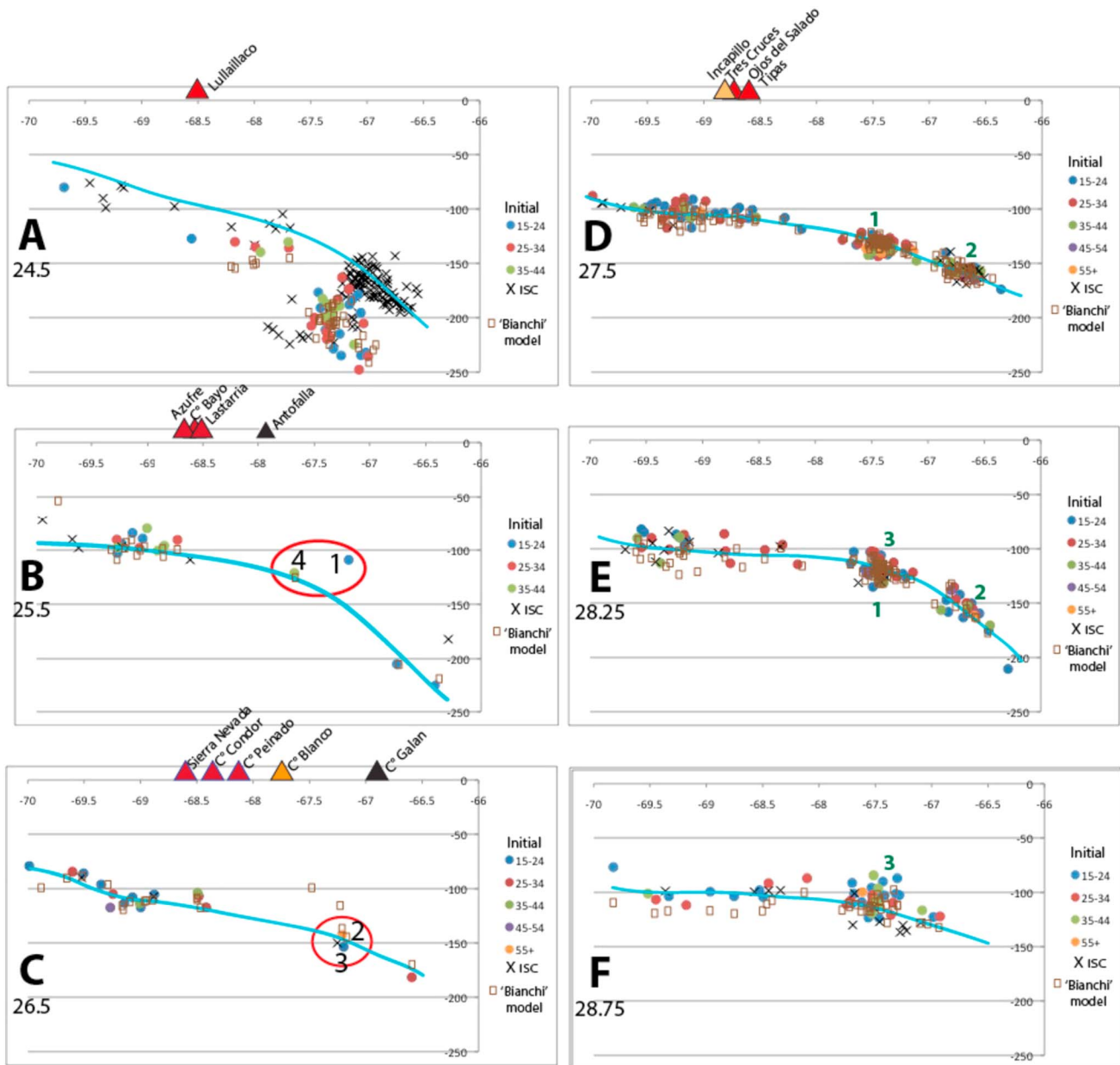


**Figure 6.** East-west cross sections of intermediate-depth seismicity across the Southern Puna array with interpreted profiles of the Wadati-Benioff zone indicated in blue. Latitudes on sections A to F are centers of profiles over which earthquakes are binned. The bins are over 1° of latitude in sections A to D and over 0.5° in sections E and F (see Figure 4). Hypocenters determined by the Southern Puna array using the default velocity model in Figure 5b are shown as colored circles coded to the number of stations used in the location. The brown squares are array of earthquakes located using the Bianchi velocity model in Figure 5b with constraints from Bianchi *et al.* [2013] and Heit *et al.* [2014]. Earthquakes located on more than 40 stations in the ISC catalog during the deployment period are shown as crosses. Triangles show major volcanic centers (red: active, violet: young, and black: older). The profile in section A is north of the Southern Puna array and is largely guided by catalog earthquakes as hypocenters located with array data are considered to be less accurate. Sections B and C show gap-filling earthquakes #1 to #4 in the Antofalla gap region. Sections D and E show locations of the Pipayaco nest earthquakes in clusters 1 and 2, and sections E and F show those in Pipayaco cluster 3. The western part of the section F profile is guided by the teleseismic earthquakes as the region is far outside of the Southern Puna array. The eastern part of the profile F is closer to the Southern Puna array and the profile considers both Southern Puna array and catalog locations.

time period, global teleseismic catalogs list only 44 earthquakes within the strict boundaries of the array with only seven meeting our good criteria. The regionally recorded events meeting our good criteria and using our initial velocity model are color coded for depth in Figure 4, and the good catalog events are shown as crosses.

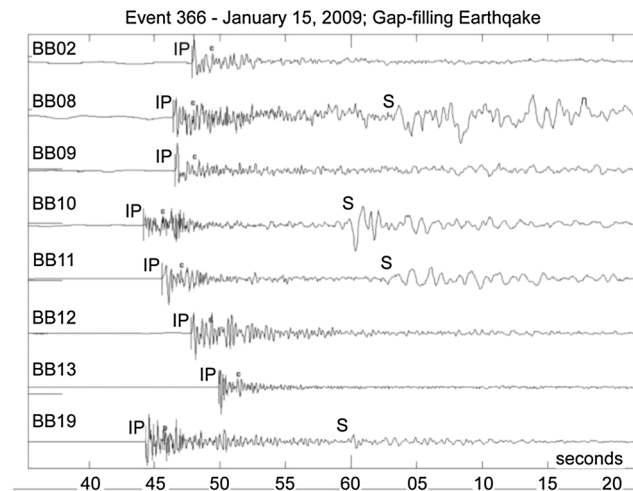


**Figure 7.** Vertical components of seismograms from stations BB02, BB08, BB09, BB10, BB11, BB12, BB13, and BB19 (locations in Figure 3) for gap-filling 15 January 2009 earthquake (#2 on Figures 4 and 8 and in profile D in Figure 6, event 366 in Appendix S2). The impulsive *P* wave (IP) and pronounced differences in amplitude or near absence of *S* waves (labeled S) are attributed to varying attenuation within the Southern Puna array.

*et al.*, 1982; *Isacks*, 1988; *Cahill and Isacks*, 1992; *Whitman et al.*, 1992, 1996; *Kirby et al.*, 1996]. During the time of the Southern Puna array, only four intermediate-depth earthquakes from this region were recorded that met our “good location” criteria. These events are numbered 1 to 4 on Figures 4 and 6 and have calculated coda magnitudes ( $M_c$ ) of 3.6 (#1 = 6 April 2008), 3.8 (#2 = 15 January 2009), 2.5 (#3 = 24 January 2009), and 3.0 (#4 = 14 February 2009). They are listed by date in Appendix S2 with locations from alternative velocity models shown in Appendix S3. Traces from earthquake #2 illustrating the impulsive *P* and poorly defined or absent *S* arrivals associated with these events are shown in Figure 7. The #2 event (15 January 2009) subsequently appeared in the ISC catalog with a  $m_b$  of 3.6–4.2 and a depth of 131–150 km, which overlap our magnitude of 3.8 and depth of 143 km from the initial velocity model.

To the north, the Antofalla teleseismic gap is bounded by the earthquakes in the Jujuy nest located between 22° and 25°S (Figures 4 and 6), which like the Antofalla gap has long been recognized in teleseismic and regional studies [e.g., *Cahill and Isacks*, 1992; *Kirby et al.*, 1996]. As seen in Figure 6 (profile A), the locations for Jujuy nest events using the Southern Puna array data are significantly deeper (approximately 25 km) than those from teleseismic studies as is also the case for all of the velocity models used in Appendix S3. Although a temporal shift in seismogenesis could be a factor (some catalog events also fall at greater depths), these events are well outside the Southern Puna array (Figure 4) and thus the locations based on array data might be expected to be less accurate in a systematic fashion. The crust above the Jujuy nest is also thicker (~60 km) [see *Yuan et al.*, 2002; *McGlashan et al.*, 2008] than that used in our initial model. As such, greater weight is given to the teleseismic data in this profile.

The Antofalla teleseismic gap is bordered to the south by the earthquakes in the Pipanaco nest [see *Cahill and Isacks*, 1992], whose spatial extent is best defined by combining Southern Puna array with global catalog data. As shown in Figures 4, 6, and 8, the Pipanaco nest can be resolved into three relatively discrete clusters, each occurring at a different depth range, with cluster 1 at ~125–140 km, cluster 2 at ~140–170 km, and cluster 3 at ~110 to 125 km. The hypocenters in clusters 1 and 2 progressively deepen away from the trench, whereas the events in cluster 3, which is farther south, occur at a relatively shallower depth (Figure 6). In detail, the hypocenter locations in cluster 1 are well constrained by the southernmost array stations on the north-south line (NS15–NS18), and those in cluster 2 are fairly well constrained by stations BB12, BB13, and BB14 located just to their north (Figures 3, 4, and 8). The hypocentral depths of the earthquakes in cluster 3 that is centered 50 km south of the array are less well constrained by Southern Puna array data. This uncertainty is expressed by an apparent increase in vertical scattering of the hypocenters of cluster 3 in Figure 6 compared with the more vertically confined hypocenters in clusters 1 and 2. Fortunately, the ISC and

Several features stand out in the distribution of the intermediate-depth earthquakes under the Southern Puna in Figures 4 and 6. One is the very sparse seismicity in the Antofalla gap region beneath the central part of the array. A second is the spatial clustering of hypocenters (earthquake nests) north of the array and along its southern boundary. A third is the concentrated seismicity near 28°S and 69°W in the general region of the Incapillo volcanic complex.

One of the most prominent aspects in the distribution of the earthquakes is the very low concentration of events at 100 to 150 km depth in the region known as the Antofalla teleseismic gap between ~25° and 27°S and 65° to 68.5°W (Figure 4). The scarcity of the events in this region is a long-recognized feature in global catalogs [e.g., *Febler*

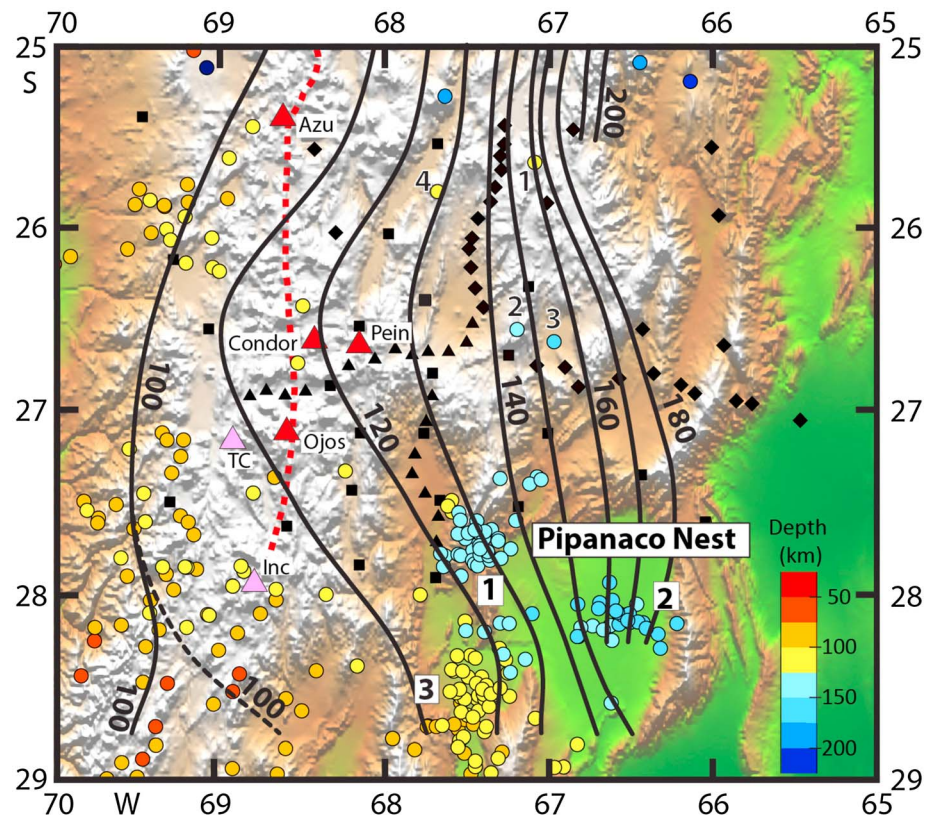


**Figure 8.** Hypocenter locations using velocity model 1 in Figure 5b for the best located mantle earthquakes below 50 km are plotted as colored circles keyed to depth. Contoured depths to the Wadati-Benioff Zone at 10 km intervals are shown in black. The contours are derived from interpolations from the earthquakes projected onto the profiles in Figure 6 as described in the text. The four intermediate-depth slab earthquakes in the Antofalla teleseismic gap at 25°–27.5°S are numbered 1 to 4. The three clusters in the Pipanaco nest are near the white-backed 1 to 3 labels. Important active volcanic centers are shown in red triangles (Ojos is Ojos del Salado, Condor is Cerro Condor, Pein is Cerro Peinado, and Azu is Cordon del Azufre), and recently, active centers are shown in pink triangles (TC is Tres Cruces and Inc is Incapillo). The red dashed line is the front of the Central Volcanic Zone (CVZ). The Southern Puna array seismic stations are shown as black squares and triangles (see Figure 3). An unlabeled contoured image is included in Appendix S4.

NEIC catalogs have more locations meeting our good criteria (crosses in Figure 6) for clusters 2 and 3 than for cluster 1. As such, we rely on Southern Puna array data in cluster 1 where catalog data are sparse and use both catalog and Southern Puna array data to define clusters 2 and 3. We note an apparent systematic vertical depth offset for events in profile F at 28.25°S (Figure 6, profile F) west of 69°S for the Bianchi velocity model relative to both initial model and ISC catalog events (see also Appendix S3). Given that this region lies south of the western Puna array stations, we put more weight on the teleseismic data in the west and use both the catalog and best Southern Puna array locations in the region of the Pipanaco nest in the east.

Another region of relatively concentrated seismicity recorded by the Southern Puna array occurs near 28°S and 69°W (Figures 4 and 6) in the general region of the Incapillo caldera, which is the southernmost volcanic center with post-Pliocene activity in the CVZ [Goss *et al.*, 2009]. Comte *et al.* [2002] also report a relatively homogeneous distribution of epicenters near and just to the west of this region based on data collected in 1988 from a 26 station array deployed onshore for 81 days and a 10 station offshore ocean bottom seismometer array (OBS) deployed for 40 days. In contrast, the region from 26.2° to 27.2°S shows relatively little local or teleseismic seismicity.

### 3.3. Construction of the Wadati-Benioff Zone Slab Contours

The method of Cahill and Isacks [1992] was employed in producing the contours shown in Figures 8–10. With this approach, the earthquakes are first separated into vertical latitudinal bins and projected onto profiles on which visual best fit curves are drawn through the center of the earthquake clusters (see Figures 4

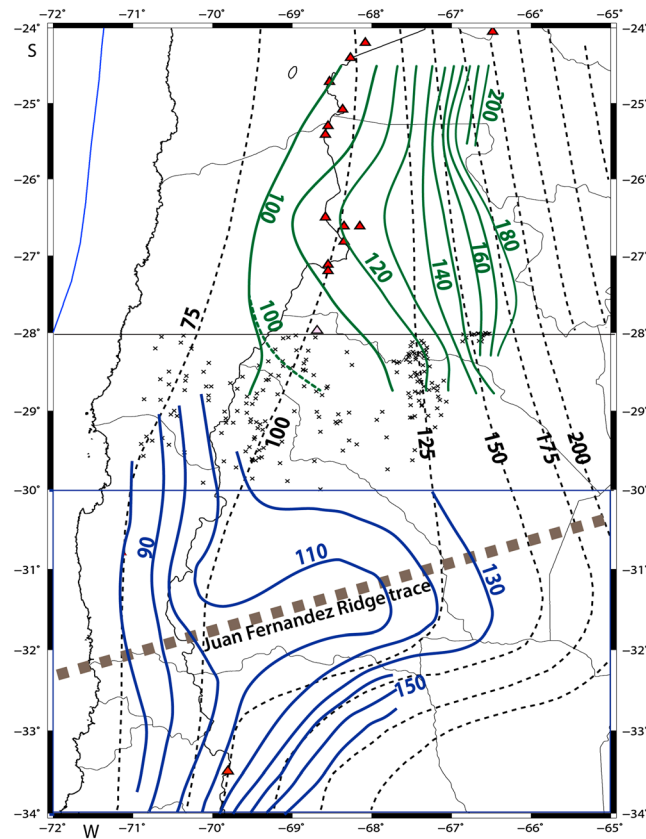


**Figure 9.** Comparison of the three sets of contours used to construct the continuous Wadati-Benioff Zone surface from 24° to 34°S at 25 km intervals in Figure 10. The Wadati-Benioff zone contours for the Southern Puna array at a 10 km interval from Figure 8 are shown in green with the dashed line labeled 100 representing the eastern edge of the 100 km contour near 28°S. The 25 km contours of Cahill and Isacks [1992] are shown as dashed lines. The 10 km contours of Anderson et al. [2007] to the slab surface south of 30°S are shown in blue with the labels shifted down 10 km to roughly approximate the center of the Wadati-Benioff zone as discussed in the text. The 199 earthquakes from 1965 to 2012 listed in the ISC catalog, which occurred between 28° and 30°S and are located on at least 40 stations, are plotted as crosses. The dashed line is the trace of the subducted Juan Fernandez ridge from Yañez et al. [2001]. Red triangles are locations of young volcanic centers in the CVZ in the north and the SVZ Tupungato volcano in the south. The Incapillo volcanic center that last erupted at ~0.5 Ma near 28°S is shown in pink.

and 6). The earthquakes on profiles A to D in Figure 6 are based on 1° latitude bins with a half degree on each side, whereas those on profiles E and F are from half degree latitude bins with a quarter degree on each side. Contours of constant depth are then drawn by connecting these profiles to create the map with a 10 km contour interval shown in Figure 8 (an unlabeled version is in Appendix S4) to the center of the earthquake concentrations (Wadati-Benioff zone).

The resulting contours are then compared in Figure 9 with the contours of Cahill and Isacks [1992] (black dashed lines) and depth-adjusted contours of Anderson et al. [2007] (blue lines) from the CHARGE array in the flat-slab region to the south (Figure 1). The published contours from Anderson et al. [2007], like the similar contours in Gans et al. [2011], which incorporate the later SIEMBRA data, require a depth adjustment before being plotted on Figure 9 as they are contours to the top of the Wadati-Benioff seismic zone, rather than contours to the center of the seismic zone as are those in Figure 8 and those in Cahill and Isacks [1992]. The shift used here is based on the assumption of an average Wadati-Benioff zone thickness of 20 km. In a strict sense, this would imply a downward translation of 10 km given a 0° slab dip and one of 14 km given a 45° slab dip (thickness of the slab divided by the cosine of the slab dip). However, given the relatively shallow dip of the Wadati-Benioff zone in the shallow part of the flat-slab region, the variability

in the Wadati-Benioff zone thickness and the uncertainties in slab dip (which also partially reflect the contouring procedure used), we have chosen to simply shift the CHARGE contours uniformly downward by 10 km.

In Figure 10, we present a synthesis that attempts to reconcile all of the contour data in Figure 9 into a single 25 contour interval map from 25° to 35°S. An unlabeled version of this map is provided in Appendix S5 and a comparison with the global reference slab 1.0 contours from Hayes et al. [2012] in Appendix S6. A perspective view of the contours in Figure 10 is shown in Figure 11 with other views provided in Appendix S7. Major discrepancies with the global reference slab 1.0 model contours in Appendix S6 can apparently largely be attributed to the lack of local network control and artifacts in the smoothing algorithm used in creating the slab 1.0 model (G. Hayes, personal communication, 2014).

The contours shown in Figures 8 and 10 differ most from those of Cahill and Isacks [1992], where those authors had little intermediate-depth teleseismic data to guide their construction. In these regions, Cahill and Isacks [2002] simply fit their contours to the simplest path given by a least squares fit (i.e., a smooth

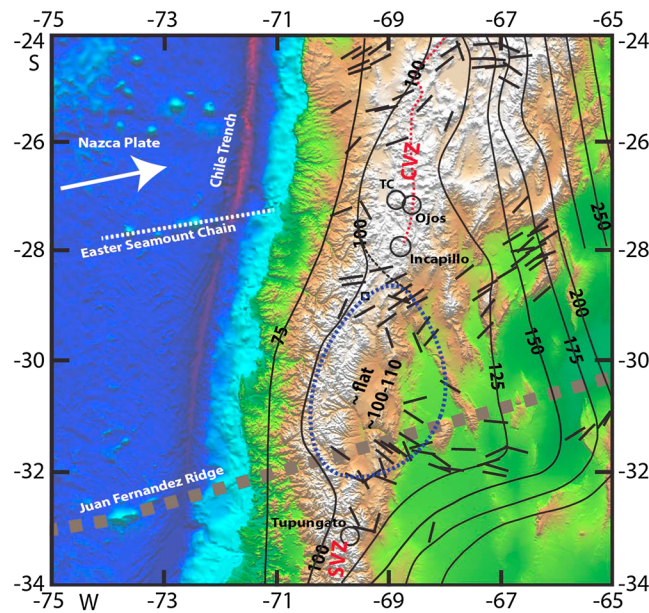


**Figure 10.** SRTM image of the Southern Puna and Chilean-Pampean flat-slab region with contours to the Wadati-Benioff Zone at 25 km interval as merged from contours in Figure 9. Contours from 28°S to 25°S are largely based on Southern Puna array data; those to the south and north and at depths over 180 km are based on combining teleseismic catalog earthquakes and the contours of *Cahill and Isacks* [1992] and *Anderson et al.* [2007] as discussed in the text. The dotted ellipse approximates the region where the Wadati-Benioff zone is near 100–110 km depth over the Chilean-Pampean flat-slab region, and the thick black lines show the horizontal projections of *T* axis orientations of published CMT solutions [Ekström et al., 2012]. The projection of the Juan Fernandez Ridge subduction path is denoted by the thick gray dashed line [Yañez et al., 2001], and the Nuvel-1 Nazca plate and South American Plate convergence direction is indicated by the white arrow [DeMets et al., 1990]. The white dotted line marks the volcanic islands of the Easter Seamount Chain that projects into the coast near 27°S. The position of the Quaternary to Recent CVZ arc is indicated by the red dotted line and northern part of the SVZ by the SVZ label. The locations of the CVZ Incapillo (Inc), Tres Cruces (TC), and Ojos del Salado (Ojos) volcanic and SVZ Tupungato volcanic centers are indicated by circles. An unlabeled contoured image is included in Appendix S5.

those in *Cahill and Isacks* [1992]. A factor in this similarity is that there are still no hypocenter locations at depths greater than ~130 km.

A further complication between 28°S and 30°S is that the slab appears to be relatively flat at a depth near 100 km so that small changes in “picked” depth result in large lateral shifts (Figure 10). This region is illustrated on Figure 10 by the deformed ellipse approximating the area where the slab appears to be quite flat. The geometry adopted near 28°S is similar to that in the S1 transection of *Pardo et al.* [2002], who based their profile on catalog teleseismic data and local array data in *Comte et al.* [2002].

Linking the Wadati-Benioff geometry of *Cahill and Isacks* [1992] and the Southern Puna array contours to the downward shifted CHARGE-SIEMBRA contours to the south results in a 25 km interval contour map that does not exhibit the pronounced northern curvature near 30°–31.5°S, which appears in the 10 km contour map of *Anderson et al.* [2007]. Although this could be partially due to a larger contour interval, we note that *Gans et al.* [2011] state that the new locations and receiver function slab depths obtained in the SIEMBRA experiment indicate that the flat region of the slab and the area of overthickened subducted oceanic crust likely extend north of where the CHARGE-SIEMBRA coverage ends at 30°S. These result are thus not in conflict with the flattened slab that we show extending much farther north in Figure 10.

course without overinterpreted deviations, breaks, or tears) connecting the areas of more dense seismicity. This resulted in a gradual transition from steeper to flatter subduction between 26° and 30°S (see Figure 9). With the addition of the Southern Puna array data, we now show shallower contours to the west between ~25.5°S and 27.5°S, somewhat similar contours to the east in the Antofalla gap region and a more rapid shoaling of the 100 to 130 km contours to the south of 27.5°S (Figures 8–10).

A problematic region in the contour map in Figure 10 is between 28°S and 30°S where earthquake locations derived from local instrumentation are not available to the west of the CVZ arc. The contours we show in this region are based on the 199 teleseismic earthquakes (crosses in Figure 9) from the 1965 to 2012 teleseismic catalogs that meet the *Cahill and Isacks* [1992] criteria of being recorded on at least 40 stations. In their analyses, *Cahill and Isacks* [1992] showed that this method of selection yielded a better combination of low hypocenter scattering and geographic coverage than other criteria based on azimuthal gap constraints, station distance, and presence of depth phases. Despite the additional data from the passing of 20 years and an increase in the number and quality of seismic stations in South America, the contours in this region remain essentially the same as

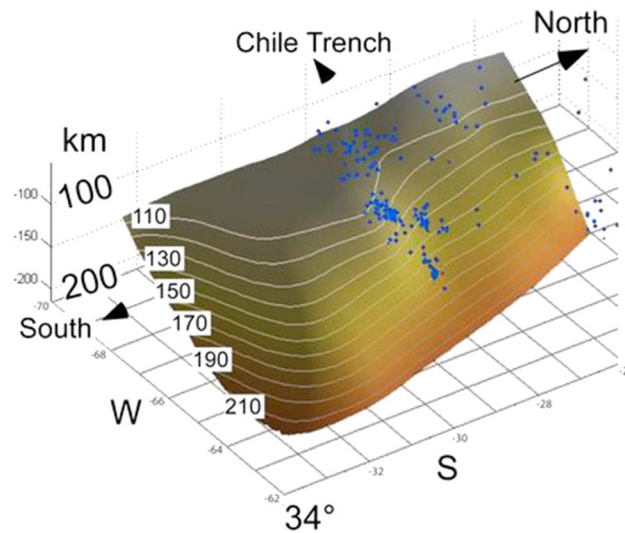


**Figure 11.** View of the three-dimensional surface representing the center of the Wadati-Benioff Zone inferred from the Southern Puna seismic project earthquake locations (blue points) and the contours of Cahill and Isacks [1992]. Earthquakes located by the Southern Puna array are superimposed. The marked seismicity centered near 28°S, which includes the three clusters of the Pipanaco nest (numbered 1 to 3), defines the shoaling point of the slab where the contours make a pronounced bend into the flat-slab region. The Antofalla teleseismic gap from ~24.5°S to 27.5°S is seen to the north. Other views are provided in Appendix S7.

earthquakes, which were calculated using the FOCMEC package included in SEISAN [Ottemöller *et al.*, 2011], are plotted in Figure 12b and listed in Table 2. First motions were picked visually on unfiltered seismograms for earthquakes with minimal hypocenter location error, sufficient azimuthal coverage, and clear phase polarity on at least 27 stations. Reported focal mechanisms are those with the best constrained solutions as indicated by a minimal variation in potential mechanisms. An example solution for the earthquake that occurred on 4 December 2008 is shown in Figure 13 with the accompanying seismograms showing the clarity of compressional and dilatational first motion picks. This earthquake was near the center of the Southern Puna array, and the solution is constrained by both good azimuthal coverage and clear first motions on 66 stations.

Mechanisms for mantle earthquakes at >50 km depth recorded on the Southern Puna array proved unreliable due to narrow array apertures relative to earthquake depth. Near-vertical raypaths from these earthquakes tended to cluster in one area of the focal sphere making well-constrained solutions from first motions unachievable. Solution averaging for spatial clusters was attempted but did not yield robust enough results to include in our interpretation of the local stress system.

## 4. Discussion

Below we use the new earthquake locations derived from the Southern Puna array to discuss the following: (a) the continuity of the subducting Nazca plate through the Antofalla teleseismic gap, (b) the relationship of the shape of the Wadati-Benioff zone to the Pipanaco earthquake nest and the arc volcanoes in the transition zone from the Southern Puna into the Chilean-Pampean flat slab, and (c) the implications of crustal earthquake distributions and focal mechanisms for the thermal condition and state of stress of the Southern Puna region crust.

### 4.1. Continuity of the Slab Through the Antofalla Teleseismic Gap and the Cause of the Gap

A long-standing question has been whether the subducting slab is continuous through the Antofalla teleseismic gap of the Southern Puna, as implied by the 3-D geometry of the Wadati-Benioff zone shown in Cahill and Isacks [1992] and the contour representations in this paper. The four numbered earthquakes with magnitudes less than  $m_c$  4.0 recorded in the teleseismic gap (Figures 4, 6, and 8) are important in this

### 3.4. Crustal Earthquake Identification and Distribution

For the 18 months that the Southern Puna network was in operation, we found 230 well-located earthquakes with hypocenters shallower than 50 km (see Appendix S2). All of these earthquakes satisfy our good criteria of being recorded on at least 15 stations and having a RMS travelt ime residual of less than 1.5 s. In the same period, the NEIC catalog shows no crustal earthquake locations meeting our selection criteria, and the ISC comprehensive catalog lists five. The locations of the good earthquakes located on the Southern Puna array are shown in Figure 12. The largest calculated magnitude ( $M_c$ ) of 3.2 for these events was registered on earthquakes on 25 January 2009 and 9 July 2009.

### 3.5. Focal Mechanism Solutions

Focal mechanism solutions for the appropriately recorded crustal

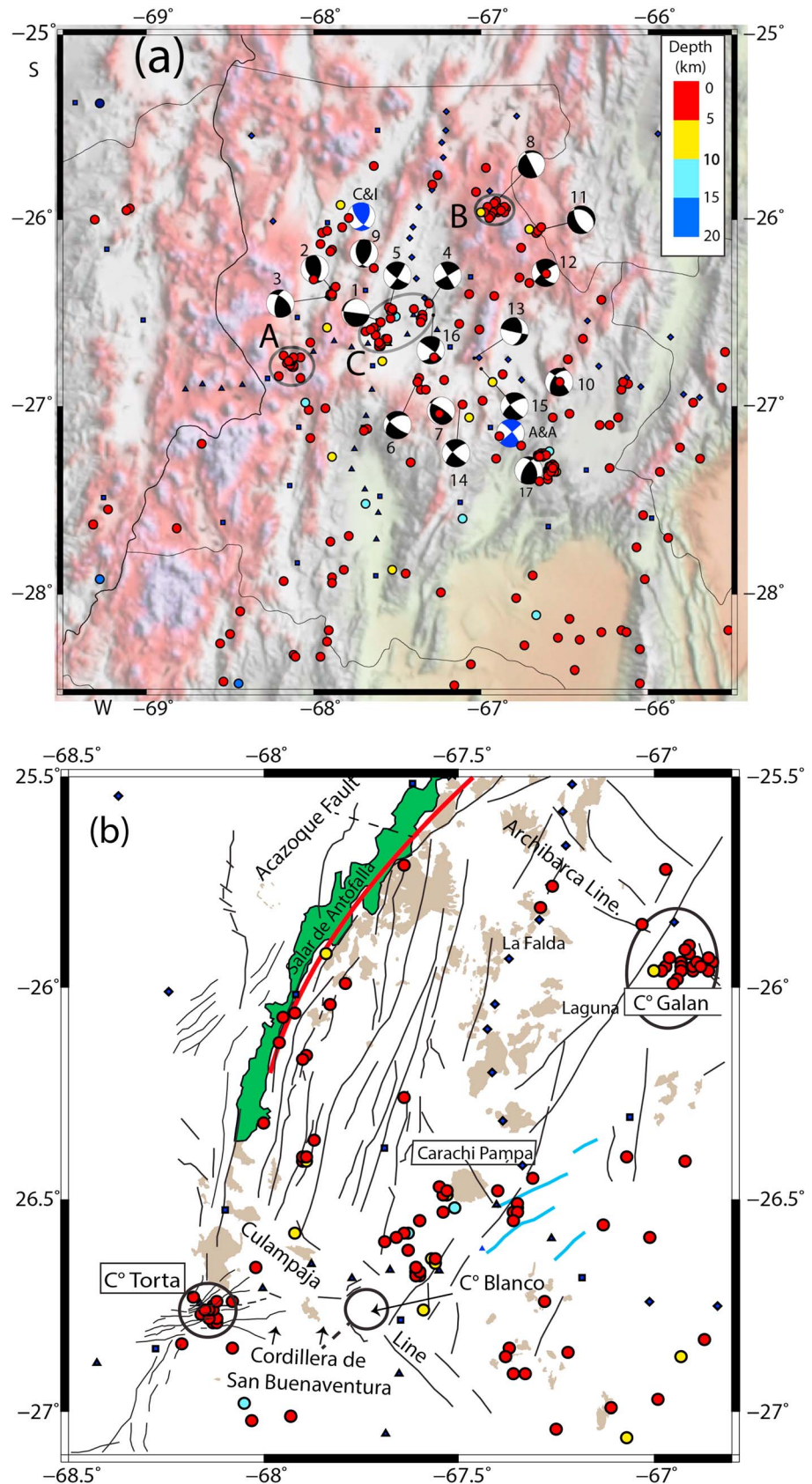


Figure 12

regard as they imply that the slab continues through this region with no significant break. Such continuity is in accord with the observation of *Cahill et al.* [1992] that no abrupt geometrical changes are required to explain the form of the slab north and south of the Antofalla gap and the observation of *Whitman et al.* [1992] that such continuity is needed for the slab to act as a guide for seismic wave propagation from the flat slab into the northern Puna.

The four earthquakes recorded within the Antofalla gap are particularly critical in defining the Wadati-Benioff contours through this region. As shown in Figure 9, these contours vary slightly from those indicated by *Cahill and Isacks* [1992]. In detail, drawing a slab surface by putting a profile through earthquakes #2 and #3 in Figure 6 (profile C), which have respective depth uncertainties of 4 and 6 km, produces a slab surface that linearly connects smoothly to hypocenters both updip and downdip of the gap. Putting a slab surface through earthquake #4, which has a depth error of 12 km, in profile B, also produces a smooth surface. The location of earthquake #1 in profile B is more problematic as the Wadati-Benioff zone would have to remain shallow and then quickly steepen to connect to the deeper earthquakes near 66.75°W. A justification for not putting a profile through earthquake #1 is also its depth uncertainty of 22 km and relatively high traveltimes residual of 1.4. A too shallow depth for earthquake #1 could be the result of local velocity heterogeneities. Support for strong attenuation of high-frequency phases in this region comes from the impulsive *P* arrivals with weak or unrecognizable *S* arrivals associated with the 2.5–3.8 magnitude earthquakes in this area (Figure 7). High attenuation in the Antofalla gap region is supported by *P* wave [*Bianchi et al.*, 2013], *S* wave [*Calixto Mory et al.*, 2013], and attenuation [*Liang et al.*, 2014] tomography.

We suggest that the virtual lack of earthquakes in the Antofalla gap is due to a relatively high temperature in the mantle wedge. Such temperatures could promote more ductile modes of failure within the slab at these depths or perhaps an updip shift for seismogenic phase changes due to dewatering updip to the west of the gap region. Such a scenario is in accord with the thermal mechanism suggested by *Kay et al.* [1994] and *Risse et al.* [2013] to explain the absence of a subducted slab signature (e.g., low La/Ta and Ba/La ratios) in young mafic Puna lavas erupted over the teleseismic gap and is in line with temperature being a primary factor in driving slab dehydration reactions [e.g., *Hacker et al.*, 2003]. Cooler slab temperatures at the same depth on the edges of the teleseismic gap in the Jujuy and Pipanaco earthquake nests to the north and south are consistent with the abundant intermediate-depth seismicity in those regions. As argued by *Kay et al.* [1994] and *Kay and Coira* [2009], the high temperature in the mantle wedge can be attributed to decompression melting following delamination of the continental lithosphere. Evidence supporting this delamination comes from the high-velocity region interpreted as a block above the subducting slab in the Antofalla teleseismic gap in tomographic images [*Bianchi et al.*, 2013; *Calixto Mory et al.*, 2013; *Liang et al.*, 2014].

#### 4.2. The Transition From the Southern Puna to the Northern Chilean-Pampean Flat Slab

The geometry of the subducting slab under the Southern Puna plateau margin and the northern flat slab in Figures 8–10, based on Southern Puna array data, differs subtly but importantly from previous renditions in shape and depth. Most importantly, the 100 to 125 km contours to the Wadati-Benioff zone show a more abrupt transition to a shallow depth farther to the north on the northern side of the Chilean-Pampean flat-slab region (Figures 8–10). The evidence for this shape comes mostly from the improved resolution of the hypocenters in the three relatively discrete clusters of the Pipanaco nests (Figures 6 and 8). Importantly, the northern two clusters progressively deepen to the east, whereas the southern cluster is at a shallower depth at the same distance to the trench. The bend in the contours and the relation to the Pipanaco clusters are well seen on the 3-D representation of the Wadati-Benioff zone surface in Figure 11.

**Figure 12.** Maps of crustal earthquakes color coded to depth. (a) Epicenter locations for the 230 best located crustal earthquakes from this study are plotted as points. Focal mechanisms from *Chinn and Isacks* [1983] and *Assumpcao and Araujo* [1993] are shown in blue, and those in black are keyed to the new events listed in Table 2. Cerro Torta and Cerro Galán swarms are in black circled areas labeled A and B, and the Cerro Blanco to Carachi Pampa regional nest is in black oval labeled C. Small black diamonds and squares are seismic stations. (b) Map of faults, major lineaments, and mafic volcanic centers (light brown) compiled from *Risse et al.* [2008], *Schnurr et al.* [2006], and *Baldwin* [2005] compared to Southern Puna array earthquake locations. Faults parallel to the linear array of earthquakes between Cerro Blanco and Carachi Pampa are in blue; others are in black. The Salar de Antofalla is shaded in green with the bounding Acazoque Fault in red. La Falda and Laguna centers are the youngest mafic volcanic centers. Cerro Torta and Cerro Galan swarms are circled.

**Table 2.** Crustal Earthquake Focal Mechanisms

Solution	Fault Type	Date	Longitude	Latitude	Depth (km)	Strike	Dip	Rake	$M_C$	Station ( $n$ )	
1		Oblique normal	8/31/08	-67.622	-26.538	< 5.0	277.5	90.0	75.0	2.4	45
2		Oblique reverse	9/27/08	-67.899	-26.365	< 5.0	144.5	44.0	60.5	2.9	54
3		Oblique reverse	10/8/08	-67.925	-26.415	0.1	310.0	54.1	37.5	2.8	47
4		Strike slip	11/7/08	-67.360	-26.53	0.1	150.0	90.0	0.0	2.8	51
5		Strike slip	12/4/08	-67.547	-26.472	1.2	125.0	77.1	7.6	2.9	66
6		Oblique normal	12/14/08	-67.381	-26.867	< 5	127.8	74.8	-48.2	2.7	57
7		Oblique reverse	1/3/09	-67.229	-27.014	4.3	304.4	75.5	75.0	2.5	38
8		Strike slip	1/4/09	-66.613	-26.285	< 5.0	137.2	62.0	-11.2	3.1	57
9		Oblique reverse	1/5/09	-67.633	-26.263	4.6	165.3	44.0	60.5	2.2	30
10		Oblique reverse	1/7/09	-66.532	-26.871	16.2	315.7	79.5	44.0	2.5	39
11		Oblique normal	1/7/09	-66.664	-26.060	< 5.0	152.3	61.1	-72.8	2.6	27
12		Oblique normal	1/25/09	-66.915	-25.908	18.2	333.3	90.0	70.0	3.2	35
13		Oblique reverse	3/7/09	-67.040	-26.743	3.9	102.3	86.5	44.9	3.0	54
14		Strike slip	5/3/09	-67.126	-26.991	12.0	133.6	80.8	-17.8	2.9	59
15		Strike slip	5/19/09	-66.998	-26.800	12.0	139.7	76.6	-22.5	3.1	62
16		Strike slip	6/24/09	-67.285	-26.513	12.0	307.1	85.5	-29.7	2.6	56
17		Oblique reverse	7/9/09	-66.715	-27.343	12.0	336.1	44.8	44.8	3.2	47

A comparison of the revised shape of the subducting slab with horizontal projections of tension ( $T$ ) axes solutions from the global centroid moment tensor (CMT) catalog [Ekström *et al.*, 2012] in Figure 10 shows a pattern of basically contour-perpendicular  $T$  axis orientations. The alignment of the  $T$  axis projections with the direction of the steepest descent of the slab is particularly apparent in the Pípanaco nest region where many  $T$  axis solutions exist. Such a correspondence provides strong support for the revised slab shape,

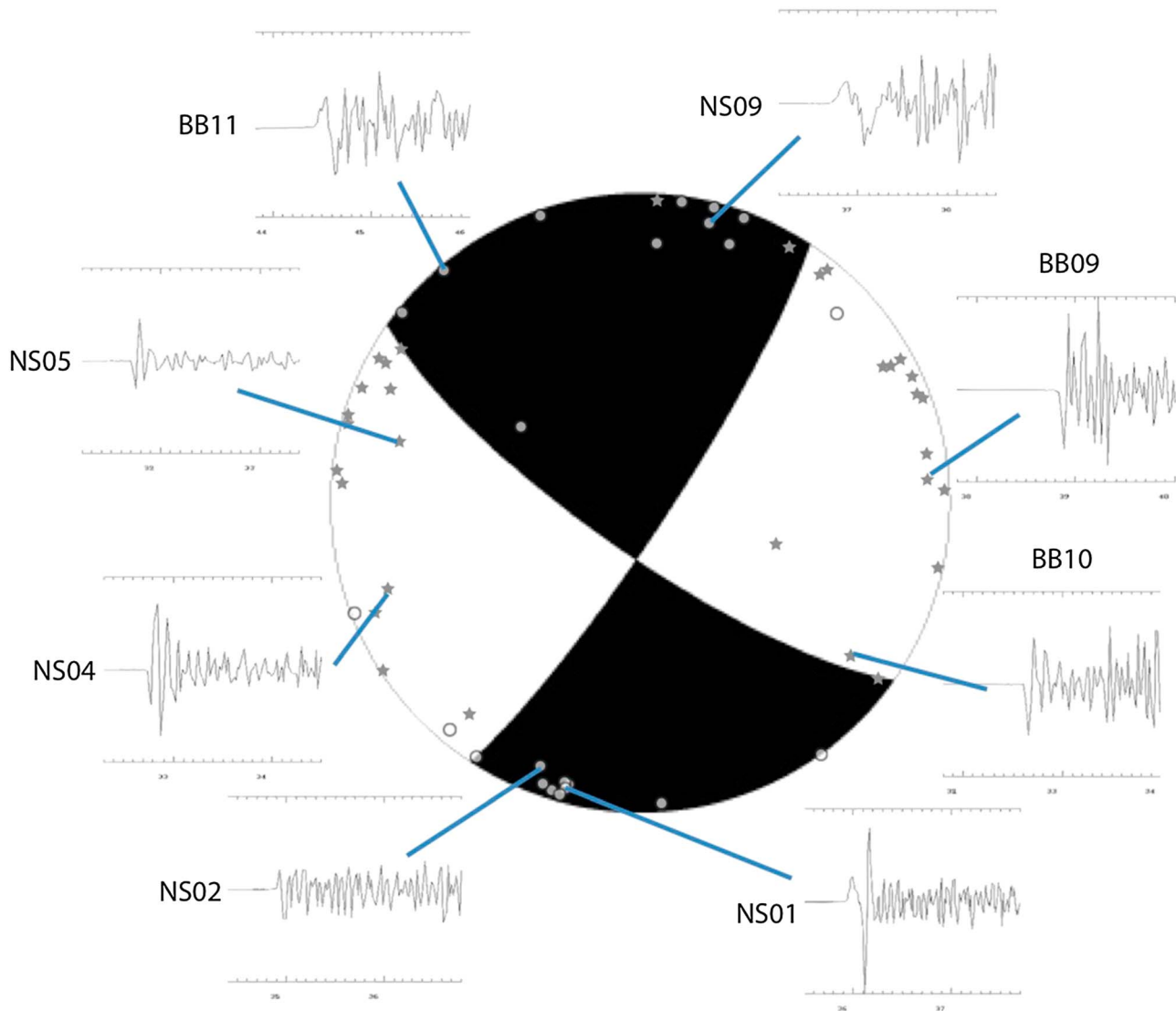


**Figure 13.** Focal mechanism solution for 4 December 2008 crustal earthquake with seismograms showing dilatational (stars) and compressional (circles) picks plotted on focal sphere. Seismograms are unfiltered and displayed at equal gain. Focal mechanism solutions for all crustal earthquakes are in Table 2.

provided that the dominant stress in the *T* axis is downdip tension. Taking a more regional perspective, the *T* axes rotate in good correspondence northward with the revised contours from a more northeast-southwest trend where the slab bends near 28°S to an average E-W orientation in the Jujuy nest region near 24°S.

The three distinct earthquake clusters in the Pípanaco nest, their focal mechanism, and their locations with respect to the revised contours suggest that these earthquakes result from additional stress imposed by slab shoaling, which could enhance localization of fluid pressure stemming from slab dehydration. The three focal points in the bend (Figures 10 and 11) would then correspond to spatially confined earthquake rupture zones. One mechanism for driving these earthquakes is the commonly suggested dehydration embrittlement process [e.g., Hacker *et al.*, 2003], which is also advocated by Anderson *et al.* [2007] to produce slab earthquakes throughout the flat-slab region. A spatial association between the Pípanaco nest earthquakes and a region of high attenuation in the Qp tomographic image in the mantle wedge just above the slab in this region in Liang *et al.* [2014] is also consistent with dehydration embrittlement.

We further note a correlation of *T* axis projections with the direction of slab dip and possible bends in other parts of the flat-slab region, where *T* axis projections would initially appear to be more chaotic (Figure 10). One region where a bend is possible is where the northwest-southeast trending alignments of *T* axes

between the 100 and 125 km contours at 28°S to 30°S parallel the eastern edge of the 100 km contour. Such a bend could follow the trend of the Sierras Pampeanas at the surface and wrap around the subducting Juan Fernandez Ridge north of the sharp bend in the *Anderson et al.* [2007] contours as would be consistent with the *T* axis marking the steepest descent and downdip tension direction in the slab. Such a geometry is also consistent with the comment in *Gans et al.* [2011] that earthquake and receiver function data from the SIEMBRA experiment indicate that the flat section of the slab extends north of 30°S.

Studies on the location and style of volcanism between the CVZ and the Chilean-Pampean flat slab have noted that the region between 27°S and 29°S is a critical area for understanding the relation between the shape of the subducting slab and arc magmatism [e.g., *Barazangi and Isacks, 1976; Kay and Mpodozis, 2002*]. The lack of post late Miocene arc volcanism from the Incapillo complex at 28°S to the Tupungato volcano near 33°S is consistent with the northern edge of the flat slab being linked to volcanism terminating at 28°S just as volcanism ends at the southern end of the flat slab north of the Tupungato volcano (Figure 10). Further, the region of concentrated seismicity near 28°S under the Incapillo caldera occurs where the 100–110 km contours bend sharply into the foreland (Figure 8) and south of the region of relatively sparse seismicity at 26.2° to 27°S. *Kirby et al.* [1996] attributed this along-strike variation in earthquakes to a variable distribution of fractures or faults in the subducting oceanic crust. However, the depths and proximity of these earthquakes relative to the swing in the 110 contour toward the foreland are also consistent with a relation between these earthquakes and a bending slab.

Another difference of our redefined geometry from previous representations in the Southern Puna is the more pronounced westward bulge of the 100 to 130 km contours in the region centered near 27°S where the Easter Seamount (or Copiapó) volcanic chain intersects the Chile Trench (Figure 10). The analyses in Appendix S3 show that this bulge is not an artifact of the choice of a velocity model. Interestingly, the Easter Seamount volcanic chain projects into the Andes at the latitude of the fore-arc Tres Cruces volcanic center, which sits east of where the E-W trending Cordillera de Buenaventura extends into the back arc (Figure 2). Some, like *González-Ferrán et al.* [1985], have long speculated on a relation between the intersection of the Easter Seamount volcanic chain and these features on the South American plate. Further, the westward bulging contours correspond to where the CVZ volcanic arc is ~105–115 km above the Wadati-Benioff zone (Figures 8–10) as opposed to at ~24°S to 21°S where the CVZ arc front east of the Salar de Atacama is ~130–140 km above the Wadati-Benioff zone [e.g., *Cahill and Isacks, 1992; Syracuse and Abers, 2006*]. The southernmost CVZ arc center (0.5 Ma Incapillo complex), which is chemically similar to the fore-arc Tres Cruces center [e.g., *Kay et al., 2013*], is located on the southern margin of the bend above the 105–110 km (Figure 8).

### 4.3. Controls on the Distribution of Crustal Earthquakes, Focal Mechanisms, and the State of Stress in the Southern Puna Region Crust

Turning to the crust, several important features of the distribution of crustal earthquakes recorded by the Southern Puna array are apparent in Figure 12. The first is that almost all events are shallower than 15 km with most in the upper 5 km. A second is that most of the earthquakes that are at depths > 10 km are in volcanically inactive regions to the south and east of the Puna, particularly in the Sierras Pampeanas (Figures 2 and 12). The third is that the crustal earthquakes mostly occurred in either two distinct seismic swarms or in trends parallel to mapped faults with a particularly large number in a persistent nest in the southeastern Puna. The cluster of events at 27.3°S and 66.6°W are due to explosions at the Bajo de Alumbrera mine.

The shallow depths of most of the crustal earthquakes recorded by the Southern Puna array point to a shallow brittle-ductile transition, which is consistent with an elevated mantle and crustal thermal structure being responsible for the low crustal velocities in the refraction model in Figure 5a. Further support for relatively high temperatures under the Southern Puna comes from attenuation and *P* and *S* tomographic images generated from Southern Puna array data [*Bianchi et al., 2013; Liang et al., 2014; Calixto Mory et al., 2013*] along with two seismic swarms.

The first of these swarms was centered on a volcanic dome complex in the Cordillera de San Buenaventura, some 15 km south of the Cerro Peinado volcano and immediately east of the active CVZ arc (Figures 2 and 12). This swarm, which lasted for about 18 h on 23 January 2009, consisted mostly of microearthquakes that are discernible only on records from station EW15 (Figure 3). The five swarm events located on multiple stations are shown in Figure 14 (see Appendix S2). Of these, the three largest ( $2.3 < m_b < 2.4$ ) are

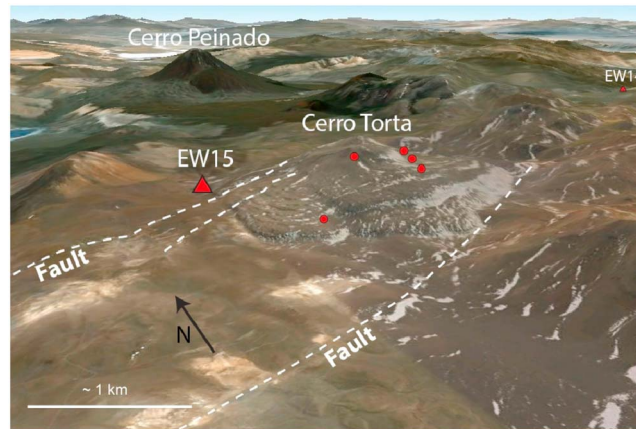


**Figure 14.** Google Earth image at elevation 4719 m looking northeast toward Cerro Torta volcanic dome. Epicenter locations for the five largest events of 23 January 2009 swarm are shown as red circles. Red triangles denote stations EW15 and EW14. Cerro Peinado is the prominent dark volcano visible to the north. Dashed lines are faults including a south dipping scarp running nearly east-west immediately south of Cerro Torta and two faults mapped by Baldwin [2005] cutting the north side of the dome.

located directly on the Cerro Torta dacitic dome. An Ar/Ar biotite age of  $0.43 \pm 0.03$  Ma [Seggiaro and Hongn, 1999] is considered to be a maximum age for this dome as biotite dates are often older than eruption ages [e.g., Hora et al., 2010]. The occurrence of the swarm near the CVZ Cerro Peinado and Ojos del Salado volcanoes is consistent with the earthquakes being related to magma movement in accord with high attenuation in the crust on tomographic images in this region [Liang et al., 2014]. Nevertheless, a relation with faulting cannot be ruled out given that three prominent east-west trending faults can be seen cutting the Cerro Torta dome in Figure 14. Baldwin [2005] has documented right-lateral strike-slip and normal fault motion on a system of east-west trending faults within

the Cordillera de San Buenaventura (Figure 12b) and suggests that the region is a transfer zone between N and NE trending strike-slip faults along the eastern side of the Maricunga Belt to the south and the Southern Puna to the north (Figure 2).

The second swarm occurred on the resurgent dome within the caldera of the ~6.5–2 Ma Cerro Galán ignimbrite complex (Figures 12b and 15) on 25 January 2009. This swarm lasted for about 17 h (see traces in Appendix S8) and showed a distinctive progression that started with a series of microearthquakes that increased in frequency over several hours to become a persistent stream of larger and more frequent events. Activity then effectively ceased for 7 h after which the largest event occurred and seismicity died off.

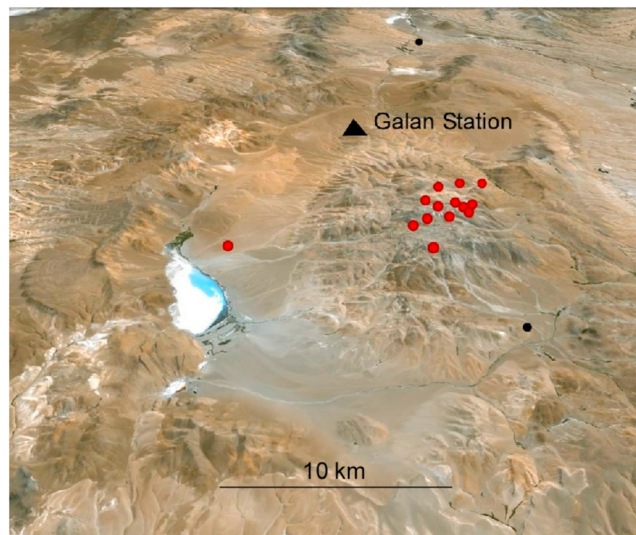


**Figure 15.** Google Earth image looking north into the Cerro Galán caldera with epicenters of the 14 largest earthquakes from the 25 January 2009 swarm shown in red. The triangle shows the Galán seismic station. Note the concentration of epicenters on the resurgent dome within the Cerro Galán caldera.

The Cerro Galán volcanic complex, in which these earthquakes occurred, is the youngest giant ignimbrite complex in the Puna with the most recent major eruption at ~2 Ma having an estimated volume of  $> 500 \text{ km}^3$  [e.g., Folkes et al., 2011]. The youngest reported age is an Ar/Ar sanidine date of 2.06 Ma from an ignimbrite that flowed to the north [Kay et al., 2011]. Small and widespread mafic cinder cones have also erupted along faults to the west of the caldera (Figure 12b) with the youngest reported ages [Risse et al., 2008] from the La Laguna (total fusion Ar/Ar age of  $0.34 \pm 0.06$  Ma) and La Falda centers (too young to date) shown in Figure 2. In line with this volcanism, the entire Cerro Galán region shows various types of seismic evidence for partial melt in the mantle and crust [Bianchi et al., 2013; Calixto Mory et al., 2013; Heit et al., 2014;

Liang *et al.*, 2014]. As such, the Cerro Galán swarm could be related to magma or hydrothermal fluid movement, although again, a link to local faulting cannot be ruled out. It is also worth noting that the ISC catalog lists four earthquakes in March of 2010 at hypocentral depths between 33 and 43.6 km with magnitudes ( $M_m$ ) from 3.4 to 4.4 beneath Cerro Galán. Such depths are in the range of partial melt zones associated with the Altiplano-Puna magma body in the northern Puna [Chmielowski *et al.*, 1999] and near depths proposed by Kay *et al.* [2010, 2011] for accumulation of partial melts of Galán magmas and by Risse *et al.* [2013] for partial crystallization of Puna mafic magmas. However, the depths of these earthquakes are not as well constrained as those located by the Southern Puna array, and they could have occurred at much shallower depths.

Another group of crustal earthquakes (Figure 12) recorded by the Southern Puna array occurred in a region of persistent activity forming a nest between the < 0.2 Ma Cerro Blanco caldera [Kraemer *et al.*, 1999] and the  $0.75 \pm 0.08$  Ma Carachi Pampa mafic cone [Risse *et al.*, 2008]. Many of these hypocenters follow a southwest-northeast trending alignment, which parallels the four fault traces shown in blue on the compilation geologic map in Figure 12b. Other hypocenters show southeast-northwest trends that also parallel mapped faults. The traces of these earthquakes align fairly well with nodal planes of strike-slip focal solutions for some Southern Puna earthquakes in Table 2 (events 4, 5, and 16).

Other groups of crustal earthquakes recorded by the Southern Puna array are aligned along the southeast side of the Salar de Antofalla (Figure 2) and appear to lie on or near the northeast trending right-lateral Acazoque strike-slip fault [Marrett *et al.*, 1994; Riller and Oncken, 2003]. The 3 November 1973  $m_b$  5.8 earthquake, which is the largest crustal event ever recorded in the Southern Puna, occurred at a depth of ~ 11 km along the Acazoque fault and has a focal mechanism (in blue on Figure 12a) indicating EW compression and NS extension [Chinn and Isacks, 1983]. Four other prominent shallow earthquakes, which occurred along the Sierra de Chango Real (Figures 2 and 12) at the border of the Puna and the Cordillera Oriental, are likely to be related to the fault system that uplifted the range. The only other published crustal focal mechanism [Assumpcao and Araujo, 1993] within the Southern Puna array region is for the < 4  $m_b$  23 June 1986 earthquake in the Cordillera Oriental east of the Sierra de Fiambala (in blue on Figure 12a).

Prior to the deployment of the Southern Puna network, only two focal mechanisms existed for crustal earthquakes in the region of the array (plotted in blue on Figure 12a). The 17 new focal mechanisms in Table 2 for the  $m_c$  2.2 to 3.2 events recorded on the Southern Puna array provide important new constraints on the modern stress system. As shown in Figure 12a, these focal mechanisms mainly show strike-slip or oblique reverse and normal fault mechanisms with most having generally east-west  $P$  axis and north-south  $T$  axis orientations. The largest deviations are for earthquakes 1, 7, 11, and 13, whose horizontal  $T$  and  $P$  axes are still within  $45^\circ$  of the average E-W and N-S orientations. Although low-magnitude earthquakes do not always reflect large-scale crustal stress, the consistency of the  $T$  and  $P$  axis orientations for the different event types and the consistency with the two preexisting mechanisms for larger events [Chinn and Isacks, 1983; Assumpcao and Araujo, 1993] support the indicated regional stress.

Interestingly, the average east-west compression and north-south extension directions for the Southern Puna crust interpreted from these focal mechanisms are consistent with the directions inferred from kinematic field observations based on fault slip data by Allmendinger [1986], Allmendinger *et al.* [1989], Marrett *et al.* [1994], and Marrett and Strecker [2000]. These authors suggested that these Southern Puna normal and strike-slip faults are due to orogen subparallel N-S extension, which they attribute to stress field changes related to diminished foreland shortening in the south compared to that farther to the north. Kraemer *et al.* [1999], Kay *et al.* [1999], Risse *et al.* [2008], Schoenbohm and Strecker [2009], and Lopez *et al.* [2010] date the beginning of this extension to the late Miocene to early Pliocene. Although a period of east-west extension between 7 and 3.5 Ma cannot be ruled out, we find no compelling evidence from focal mechanisms in the Southern Puna region for east-west extension at present.

## 5. Conclusions

The analysis of mantle and crustal earthquakes recorded during the Southern Puna seismic experiment leads to a refinement in the shape of the Wadati-Benioff zone under the Southern Puna and the northern margin of the Chilean-Pampean flat slab and supports a hot crust and mantle wedge under the Southern Puna. Some key conclusions are as follows:

1. The lack of teleseismically recorded intermediate-depth slab seismicity in the Antofalla teleseismic gap under the Southern Puna (25° to 27.5°S) is partially filled by four earthquakes with coda magnitudes of 2.5, 3.0, 3.6, and 3.8 and with emergent *P* and variably weak *S* phases. These earthquakes, along with recent tomographic images, suggest that the slab is continuous through this region. The small magnitude of these earthquakes and the teleseismic gap are interpreted as being due to a locally elevated mantle wedge temperature that may have caused the slab to dehydrate updip, leaving a fluid-deficient slab under the Antofalla gap. This interpretation is in accord with eruption of intraplate mafic lavas that lack a slab signature above the gap.
2. A revised slab geometry under the Southern Puna and northernmost Chilean-Pampean flat-slab region shows a more abrupt shallowing of the Nazca plate farther to the north than in previous models. Important evidence for this revised shape comes from the three mantle earthquake clusters in the Pipanaco nest (27.5–29°S, 68–66°W), whose locations are consistent with being related to dehydration associated with localized slab bending. Additional support for the revised geometry comes from the near-normal orientation of published horizontal projections of *T* axes to the revised contours. The revised more northerly bend in the flat slab also occurs just south of the Pleistocene CVZ Incapillo volcanic center, which is the last arc volcano with post-Miocene activity until reaching the SVZ Tupungato volcano to the south of the flat slab.
3. A westward indentation in the 100 to 130 km Wadati-Benioff zone contours at 25.5°S to 27.5°S spatially projects into the subducting Easter Seamount volcanic chain on the Nazca plate.
4. A preponderance of low-magnitude crustal earthquakes (<3.2 *M<sub>c</sub>*) in the Southern Puna at depths under 5 km is consistent with a hot crust and a shallow brittle-ductile transition. Short-duration swarms on the < 0.3 Ma Cerro Torta dome near the CVZ volcanic front and within the caldera of the 6–2 Ma Cerro Galán complex above the Antofalla teleseismic gap are interpreted as reflecting fluid or magma movement and/or slip along preexisting faults.
5. Shallow earthquakes (most < 5 km) in a persistent nest between the Cerro Blanco and Carachi Pampa volcanic centers are generally aligned parallel to known faults as are those near the Acazoque and Sierra de Chango Real faults. Focal mechanisms for 17 of these crustal earthquakes, along with the only two previously published events, show right-lateral strike-slip, oblique reverse, and oblique normal motion that is predominantly defined by north-south extension with east-west shortening. This stress alignment both mirrors that deduced from fault kinematics on late Neogene structures by others and shows that the Southern Puna is not currently subject to east-west extension.
6. The character of mantle and crustal seismicity in the Antofalla teleseismic gap area in the region of the Cerro Galan caldera is consistent with tomographic evidence for recent crustal and mantle lithospheric delamination under the Southern Puna.

#### Acknowledgments

Funding for this project came from U.S. National Science Foundation grant EAR-0538112 and the German Research Centre for Geosciences and German Research Council (DFG). Instruments were provided by IRIS-PASSCAL, Universities of Missouri and St. Louis, and the German GeoForschungsZentrum. We thank all of those who participated in field work, logistics, and data processing including A. Perez, D. Comte, N. McGlashan, M. Fort, G. Chavez, P. Alvarado, G. Monsalvo, J. Quinteros, J. Mamaní, J. Reynoso, M. Montivero, R. Fu, R. Kay, D. Robinson, N. Cosentino, T. Lupo, S. Ramirez, M. Spagnuolo, F. Calixto, R. Alonso, J. Valenzuela, N. Groos, A. Cabolova, SERNAMIN, INPRES, and the Argentine military and citizens of Catamarca Province, Argentina. Two anonymous reviewers and the Editors provided suggestions that improved the manuscript.

#### References

- Allmendinger, R. W. (1986), Tectonic development, southeastern border of the Puna Plateau, northwestern Argentine Andes, *Geol. Soc. Am. Bull.*, *97*, 1070–1082.
- Allmendinger, R. W., M. Strecker, J. E. Eremchuk, and P. Francis (1989), Neotectonic deformation of the Southern Puna plateau, NW Argentina, *J. South Am. Earth Sci.*, *2*, 111–130, doi:10.1016/0895-9811(89)90040-0.
- Allmendinger, R. W., T. E. Jordan, S. M. Kay, and B. L. Isacks (1997), The evolution of the Altiplano-Puna plateau of the Central Andes, *Annu. Rev. Earth Planet. Sci.*, *25*, 139–174, doi:10.1146/annurev.earth.25.1.139.
- ANCORP Working Group (2003), Seismic imaging of a convergent continental margin and plateau in the central Andes (Andean Continental Research Project 1996 ANCORP '96, *J. Geophys. Res.*, *108*(B7), 2328, doi:10.1029/2002JB001771.
- Anderson, M., P. Alvarado, G. Zandt, and S. Beck (2007), Geometry and brittle deformation of the subducting Nazca Plate, Central Chile and Argentina, *Geophys. J. Int.*, *171*, 419–434, doi:10.1111/j.1365-246X.03483.x.
- Assumpcao, M., and M. Araujo (1993), Effect of the Altiplano-Puna plateau, South America, on the regional intraplate stresses, *Tectonophysics*, *221*, 475–496.
- Baldwin, A. K. (2005), Pliocene-Quaternary deformation and magmatism at the southern margin of the Puna plateau, Argentine Andes [MS thesis]: University at Texas at Austin, Austin, Tex.
- Barazangi, M., and B. L. Isacks (1976), Spatial distribution of earthquakes and subduction of the Nazca Plate beneath South America, *Geology*, *4*, 686–692, 1976.
- Beck, S., and G. Zandt (2002), The nature of orogenic crust in the central Andes, *J. Geophys. Res.*, *107*(B10), 2230, doi:10.1029/2000JB000124.
- Bianchi, M., B. Heit, A. Jakovlev, X. Yuan, S. M. Kay, R. N. Alonso, E. A. Sandvol, and R. Kind (2013), Teleseismic tomography of the Southern Puna plateau in Argentina and adjacent regions, *Tectonophysics*, *586*, 65–83.
- Bondar, I., S. C. Myers, E. R. Engdahl, and E. A. Bergman (2004), Epicentre accuracy based on seismic network criteria, *Geophys. J. Int.*, *156*, 483–496, doi:10.1111/j.1365-246X.2004.02070.x.
- Cahill, T., and B. L. Isacks (1992), Seismicity and shape of the subducted Nazca Plate, *J. Geophys. Res.*, *97*, 17,503–17,529, doi:10.1029/92JB00493.

- Cahill, T. A., B. L. Isacks, D. Whitman, J.-L. Chatelain, A. Perez, and J. Chiu (1992), Seismicity and tectonics in Jujuy Province, northwestern Argentina, *Tectonics*, *11*, 944–959, doi:10.1029/92TC00215.
- Calixto Mory, F. J., E. A. Sandvol, S. M. Kay, P. Mulcahy, B. Heit, X. Yuan, B. Coira, D. Comte, and P. M. Alvarado (2013), Velocity structure beneath the Southern Puna plateau: Evidence for delamination, *Geochem. Geophys. Geosyst.*, *14*, doi:10.1002/ggge.20266.
- Chinn, D. S., and B. L. Isacks (1983), Accurate source depths and focal mechanisms of shallow earthquakes in western South America and the New Hebrides Island arc, *Tectonics*, *2*, 529–563, doi:10.1029/TC002i006p00529.
- Chmielowski, J., G. Zandt, and C. Haberland (1999), The central Andean Altiplano-Puna magma body, *Geophys. Res. Lett.*, *26*, 783–786, doi:10.1029/1999GL900078.
- Coira, B., and N. Pezzutti (1976), Vulcanismo cenozoico en el ámbito de La Puna catamarqueña (25°30′–25°50′ Lat. S. y 68°–68°30′ Long. O.), *Asoc. Geol. Argent. Rev.*, *31*, 33–52.
- Coira, B., S. M. Kay, and J. Viramonte (1993), Upper Cenozoic magmatic evolution of the Argentine Puna—A model for changing subduction geometry, *Int. Geol. Rev.*, *35*, 677–720.
- Comte, D., H. Haessler, D. Louis, M. Pardo, T. Monfret, A. Lavenue, B. Pontoise, and Y. Hello (2002), Seismicity and stress distribution in the Copiapó, northern Chile subduction zone using combined on- and off-shore seismic observations, *Phys. Earth Planet. Inter.*, *123*, 197–217.
- DeMets, C., R. G. Gordon, D. F. Argus, and S. Stein (1990), Current plate motions, *Geophys. J. Int.*, *101*, 425–478.
- Ekström, G., M. Nettles, and A. M. Dziewoński (2012), The global CMT project 2004–2010: Centroid-moment tensors for 13,017 earthquakes, *Phys. Earth Planet. Inter.*, *200–201*, 1–9.
- Febre, J. N., B. Baldi, J. C. Gasco, M. Marmani, and C. Composiello (1982), *La Anomalía Geotérmica Calchaquí en el Noroeste Argentina: Un Nuevo Proceso Geodinámico Asociado a la Subducción de la Placa de Nazca*, pp. 691–703, V Congreso Latinoamericano de Geología, Argentina, Actas III.
- Folkes, C. B., H. M. Wright, R. A. F. Cas, S. de Silva, C. Lesti, and J. G. Viramonte (2011), A re-appraisal of the stratigraphy and deposit volumes in the Cerro Galán volcanic system, NW Argentina, *Bull. Volcanol.*, *73*, 1455–1486, doi:10.1007/s00445-011-0511-y.
- Gans, C., S. Beck, G. Zandt, H. Gilbert, P. Alvarado, M. Anderson, and L. Linkimer (2011), Continental and oceanic crustal structure of the Pampean flat slab region, western Argentina, using receiver function analysis: New high-resolution results, *Geophys. J. Int.*, *186*, 45–58.
- González-Ferrán, O., P. E. Baker, and D. C. Rex (1985), Tectonic-volcanic discontinuity at latitude 27° South, Andean Range, associated with Nazca plate subduction, *Tectonophysics*, *112*, 423–441.
- Goss, A. R., S. M. Kay, C. Mpodozis, and B. S. Singer (2009), The Incapillo caldera and dome complex (~28°S): A stranded magma chamber over a dying Andean arc, *J. Volcanol. Geotherm. Res.*, *184*, 384–404.
- Goss, A. R., S. M. Kay, and C. Mpodozis (2013), Andean adakites from the northern edge of the Chilean-Pampean flat slab (27–28.5°S) associated with frontal arc migration and forearc subduction erosion, *J. Petrol.*, *54*, 2193–2234, doi:10.1093/petrology/egt044.
- Graeber, F. M., and G. Asch (1999), Three-dimensional models of P wave velocity and P-to-S velocity ratio in the southern central Andes by simultaneous inversion of local earthquake data, *J. Geophys. Res.*, *104*, 237–256.
- Gudmundsson, O., and M. Sambridge (1998), A regionalized upper mantle (RUM seismic model), *J. Geophys. Res.*, *103*, 7121–7136, doi:10.1029/97JB02488.
- Hacker, B. R., S. M. Peacock, G. A. Abers, and S. D. Holloway (2003), Subduction factory 2. Are intermediate-depth earthquakes in subducting slabs linked to metamorphic dehydration reactions?, *J. Geophys. Res.*, *108*(B1), 2030, doi:10.1029/2001JB001129.
- Hayes, G. P., D. J. Wald, and R. L. Johnson (2012), Slab1.0: A three-dimensional model of global subduction zone geometries, *J. Geophys. Res.*, *117*, B01302, doi:10.1029/2011JB008524.
- Heit, B., I. Koulakov, G. Asch, X. Yuan, R. Kind, I. Alcocer-Rodríguez, S. Tawackoli, and W. Wilke (2008), More constraints to determine the seismic structure beneath the Central Andes at 21°S using teleseismic tomography analysis, *J. South Am. Earth Sci.*, *25*, 22–36.
- Heit, B., M. Bianchi, X. Yuan, S. M. Kay, E. Sandvol, P. Kumar, R. Kind, R. N. Alonso, L. D. Brown, and D. Comte (2014), Structure of the crust and the lithosphere beneath the Southern Puna plateau from seismic receiver functions, *Earth Planet. Sci. Lett.*, *185*, 1–11.
- Hora, J., B. S. Singer, B. R. Jicha, B. L. Beard, C. M. Johnson, S. de Silva, and M. Salisbury (2010), Volcanic biotite-sanidine <sup>40</sup>Ar/<sup>39</sup>Ar age discordances reflect Ar partitioning and pre-eruption closure in biotite, *Geology*, *38*, 923–926.
- Husen, S., E. Kissling, E. Flueh, and G. Asch (1999), Accurate hypocenter determination in the seismogenic zone of the subducting Nazca plate in northern Chile using a combined on-/offshore network, *Geophys. J. Int.*, *138*, 687–701.
- International Seismological Centre (2010), Reference event bulletin, International Seismological Centre, Thatcham, U. K. [Available at <http://www.isc.ac.uk/>]
- Isacks, B. L. (1988), Uplift of the Central Andean Plateau and bending of the Bolivian Orocline, *J. Geophys. Res.*, *93*, 3211–3231, doi:10.1029/JB093iB04p03211.
- Kay, R. W., and S. M. Kay (1993), Delamination and delamination magmatism, *Tectonophysics*, *219*, 177–189, doi:10.1016/0040-1951(93)90295-U.
- Kay, S. M., and B. L. Coira (2009), Shallowing and steepening subduction zones, continental lithospheric loss, magmatism, and crustal flow under the Central Andean Altiplano-Puna Plateau, in *Shallow Subduction, Plateau Uplift and Ridge and Terrane Collision*, vol. 204, edited by S. M. Kay, V. A. Ramos, and W. R. Dickinson, pp. 228–259, Geol. Soc. Am., Boulder, Colo., doi:10.1130/20091204(11).
- Kay, S. M., and C. Mpodozis (2002), Magmatism as a probe to the Neogene shallowing of the Nazca plate beneath the modern Chilean flat slab, *J. South Am. Earth Sci.*, *15*, 39–59.
- Kay, S. M., B. L. Coira, and J. Viramonte (1994), Young mafic back-arc volcanic rocks as indicators of continental lithospheric delamination beneath the Argentine Puna Plateau, Central Andes, *J. Geophys. Res.*, *99*, 24,323–24,339, doi:10.1029/94JB00896.
- Kay, S. M., C. Mpodozis, and B. L. Coira (1999), Magmatism, tectonism and mineral deposits of the Central Andes (22°–33°S latitude), in *Geology and Ore Deposits of the Central Andes*, Spec. Publ., vol. 7, edited by B. J. Skinner, pp. 27–59, Society of Economic Geology, Littleton, Colo.
- Kay, S. M., B. L. Coira, P. J. Caffee, and C.-H. Chen (2010), Regional chemical diversity, crustal and mantle sources and evolution of the Neogene Puna plateau ignimbrites of the Central Andes, *J. Volcanol. Geotherm. Res.*, *198*, 81–111.
- Kay, S. M., B. Coira, G. Woerner, R. W. Kay, and B. S. Singer (2011), Geochemical, isotopic and single crystal <sup>40</sup>Ar/<sup>39</sup>Ar age constraints on the evolution of the Cerro Galán ignimbrites, *Bull. Volcanol.*, *73*, 1487–1511, doi:10.1007/s00445-010-0410-7.
- Kay, S. M., C. Mpodozis, and M. Gardeweg (2013), Magma sources and tectonic setting of Central Andean andesites (25.5°–28°S) related to crustal thickening, forearc subduction erosion and delamination, in *Orogenic Andesites and Crustal Growth*, edited by A. Gomez-Tuena, S. M., Straub, and G. F. Zellmer, *Geol. Soc. London Spec. Publ.*, *385*, 303–334, doi:10.1144/SP385.11.
- Kirby, S., E. R. Engdahl, and R. Denlinger (1996), Intermediate depth, intraslab earthquakes and arc volcanism as physical expressions of crustal and uppermost mantle metamorphism in subducting slabs, in *Subduction From Top to Bottom*, *Geophys. Monogr.*, vol. 96, edited by G. D. Bebout et al., pp. 195–214, AGU, Washington D. C.

- Kraemer, B., D. Adelman, M. Alten, W. Schnurr, K. Erpenstein, E. Kiefer, P. van den Bogaard, and K. Gorler (1999), Incorporation of the Paleogene foreland into the Neogene Puna plateau: The Salar de Antofalla area, NW Argentina, *J. South Am. Earth Sci.*, *12*, 157–182, doi:10.1016/S0895-9811(99)00012-7.
- Lay, T., and T. C. Wallace (1995), *Modern Global Seismology*, Academic Press, San Diego, Calif.
- Liang, X., E. A. Sandvol, S. M. Kay, B. Heit, X. Yuan, P. Mulcahy, C. Chen, L. D. Brown, D. Comte, and P. Alvarado (2014), Delamination of Southern Puna lithosphere from body wave attenuation tomographic images, *J. Geophys. Res. Solid Earth*, *119*, 549–566, doi:10.1002/2013JB010309.
- Lienert, B. R., and J. Haskov (1995), A computer program for locating earthquakes both locally and globally, *Seismol. Res. Lett.*, *66*, 26–36.
- Lopez, M. C., F. D. Hongn, M. R. Strecker, R. Marrett, R. Seggiaro, and M. Sudo (2010), Late Miocene-early Pliocene onset of N-S extension along the southern margin of the Central Andean Plateau: Evidence from magmatic, geochronological and structural observations, *Tectonophysics*, *494*, 48–63.
- Marrett, R. A., and M. R. Strecker (2000), Response of intracontinental deformation in the central Andes to late Cenozoic reorganization of South American Plate motions, *Tectonics*, *19*, 452–467, doi:10.1029/1999TC001102.
- Marrett, R. A., R. W. Allmendinger, R. N. Alonso, and R. E. Drake (1994), Cenozoic tectonic evolution of the Puna Plateau and adjacent foreland, northwestern Argentine Andes, *J. South Am. Earth Sci.*, *7*, 179–207.
- McGlashan, N., L. D. Brown, and S. M. Kay (2008), Crustal thicknesses in the Central Andes from teleseismically recorded depth phase precursors, *Geophys. J. Int.*, *175*, 1013–1022.
- Oncken, O., D. Hindle, J. Kley, K. Elger, P. Victor, and K. Schemmann (2006), Deformation of the Central Andean upper plate system—Facts, fiction, and constraints for plateau models, in *The Andes—Active Subduction Orogeny*, edited by O. Oncken et al., pp. 29–44, Springer, Berlin.
- Ottmøller, L., P. Voss, and J. Havskov (2011), *SEISAN Earthquake Analysis Software for WINDOWS, SOLARIS, LINUX and MACOSX*, Department of Earth Science, Univ. of Bergen, Bergen, Norway.
- Pardo, M., D. Comte, and T. Monfret (2002), Seismotectonic and stress distribution in the central Chile subduction zone, *J. South Am. Earth Sci.*, *15*, 11–22.
- Richards, J. P., T. Ulrich, and R. Kerrick (2006), The late Miocene Quaternary Antofalla volcanic complex, Southern Puna, NW Argentina: Protracted history, diverse petrology and economic potential, *J. Volcanol. Geotherm. Res.*, *152*, 197–239.
- Riller, U., and O. Oncken (2003), Growth of the Central Andean Plateau by tectonic segmentation is controlled by the gradient in crustal shortening, *J. Geol.*, *111*, 367–384.
- Risse, A., R. B. Trumbull, B. L. Coira, S. M. Kay, and P. van den Bogaard (2008), <sup>40</sup>Ar/<sup>39</sup>Ar geochronology of mafic volcanism in the back-arc region of the Southern Puna plateau, Argentina, *J. South Am. Earth Sci.*, *26*, 1–15.
- Risse, A., R. B. Trumbull, S. M. Kay, B. L. Coira, and R. Romer (2013), Multi-stage evolution of late Neogene mantle-derived magmas from the Central Andes backarc in the Southern Puna plateau of Argentina, *J. Petrol.*, doi:10.1093/petrology/egt038.
- Schnurr, W. B. W., A. Risse, R. B. Trumbull, and K. Munier (2006), Digital geological map of the southern and central Puna plateau, NW Argentina, in *The Andes—Active Subduction Orogeny*, edited by O. Oncken et al., pp. 563–564, Springer, Berlin.
- Schoenbohm, L. M., and M. R. Strecker (2009), Normal faulting along the southern margin of the Puna Plateau, northwest Argentina, *Tectonics*, *28*, TC5008, doi:10.1029/2008TC002341.
- Schurr, B., A. Rietbrock, G. Asch, R. Kind, and O. Oncken (2006), Evidence for lithospheric detachment in the central Andes from local earthquake tomography, *Tectonophysics*, *415*, 203–223.
- Seggiaro, R. E., and F. D. Hongn (1999), Influencia tectónica en el volcanismo Cenozoico del noroeste argentino, *Acta Geol. Hisp.*, *34*, 227–242.
- Sparks, R. S. J., P. W. Francis, R. D. Hamer, R. J. Pankhurst, L. L. O’Callaghan, R. S. Thorpe, and R. S. Page (1985), Ignimbrites of the Cerro Galán caldera, NW Argentina, *J. Volcanol. Geotherm. Res.*, *24*, 205–248.
- Swenson, J., S. Beck, and G. Zandt (2000), Crustal structure of the Altiplano from broadband regional waveform modeling: Implications for the composition of thick continental crust, *J. Geophys. Res.*, *105*, 607–621, doi:10.1029/1999JB900327.
- Syracuse, E. M., and G. A. Abers (2006), Global comparisons of variations in slab depth beneath arc volcanoes and implications, *Geochem. Geophys. Geosyst.*, *7*, Q05017, doi:10.1029/2005GC001045.
- Tassara, A., H. J. Gotze, S. Schmidt, and R. Hackney (2006), Three-dimensional density model of the Nazca plate and the Andean continental margin, *J. Geophys. Res.*, *111*, B09404, doi:10.1029/2005JB003976.
- Whitman, D. (1994), Moho geometry beneath the eastern margin of northwest Argentina and its implications to the elastic thickness of the Andean foreland, *J. Geophys. Res.*, *99*, 15,277–15,289, doi:10.1029/94JB00342.
- Whitman, D., B. L. Isacks, J. L. Chalelain, J. M. Chiu, and A. Perez (1992), Attenuation of high-frequency seismic waves beneath the Central Andean Plateau, *J. Geophys. Res.*, *97*, 19,929–19,947, doi:10.1029/92JB01748.
- Whitman, D., B. L. Isacks, and S. M. Kay (1996), Lithospheric structure and along-strike segmentation of the central Andean Plateau: Seismic Q, magmatism, flexure, topography and tectonics, *Tectonophysics*, *259*, 29–40, doi:10.1016/0040-1951(95)00130-1.
- Woelbern, I., B. Heit, X. Yuan, G. Asch, R. Kind, J. Viramonte, S. Tawackoli, and H. Wilke (2009), Receiver function images from the Moho and the slab beneath the Altiplano and Puna plateaus in the Central Andes, *Geophys. J. Int.*, *177*, 296–308, doi:10.1111/j.1365-246X.2008.04075.x.
- Yañez, G. A., C. R. Ramiro, R. von Huene, and J. Diaz (2001), Magnetic anomaly interpretation across the southern Central Andes (32°–34°S): The role of the Juan Fernandez Ridge in the late Tertiary evolution of the margin, *J. Geophys. Res.*, *106*, 6325–6345, doi:10.1029/2000JB900337.
- Yuan, X., S. V. Sobolev, and R. Kind (2002), Moho topography in the Central Andes and its geodynamic implications, *Earth Planet. Sci. Lett.*, *199*, 389–402, doi:10.1016/S0012-.